ABSTRACT

KHAN, NABIL SALIH. A Data-driven Muscle-tendon Modeling Framework to Evaluate Muscle-level Performance of Ankle Exoskeletons during Human Walking. (Under the direction of Dr. Gregory Sawicki.)

It is unclear whether the biological ankle is configured to optimize metabolic economy during walking. We constructed a simplified computer model of the major ankle plantar flexors to examine the influence of muscle morphology on muscle-tendon interaction dynamics, muscle activation requirements, and metabolic energy expenditure during walking. We hypothesized that among all possible muscle configurations capable of producing 'human-like' walking mechanics when cycled with a healthy ankle angle profile, the more compliant solutions would improve metabolic economy the most. Using a uniarticular muscle model with blended triceps surae architecture and contraction capability, we varied the stiffness of the series elastic tissues(SEE), total slack length of the muscle tendon unit(MTU), and contractile element(CE) to MTU length ratio to determine the morphology combination that produced a moment profile most similar to experimental ankle moment data for walking at preferred walking speed. Experimental human muscle architecture data was used to enforce a CE to MTU length ratio and define a 'human-like' plantar flexor moment with the corresponding morphology $\vec{M}_{bio}$. Among morphology solutions that produced moment profiles equal to or better than $\vec{M}_{bio}$, compliance was inversly related to metabolic expenditure. The most metabolically economic solution of the set was morphology configuration $\vec{M}_{abs}$, which produced a 'human-like' moment with 71.8% less metabolic expenditure and was 37.8% more compliant than the human $\vec{M}_{bio}$ configuration.

In Chapter 2, we added a passive elastic exoskeleton in parallel to the blended model configured with the $\vec{M}_{bio}$ morphology defined in Chapter 1. We posited that increasing the spring stiffness of the ankle exoskeleton would induce two effects: (1) higher exoskeleton stiffness would result in larger reductions in the metabolic cost of the plantarflexors during walking; and (2) elastic ankle exoskeletons would disrupt the normal catapult mechanism exhibited by the ankle plantarflexors in unassisted walking. Simulating many combinations of biological muscle activation and exoskeleton parallel spring stiffness allowed us to predict the impact of assistance on external/internal forces, muscle-tendon dynamics, muscle activation profiles, mechanical power outputs of the MTU, CE and SEE, and metabolic cost. The model demonstrated that stiffer ankle exoskeleton springs resulted in larger decreases in plantarflexor metabolic energy consumption. However, in the process of unloading the MTU to facilitate a reduction in metabolic energy, the CE increasingly lengthened and caused the attenuation of the elastic recoil indicative of a tuned 'catapult-like' muscle-tendon interaction.

A Data-driven Muscle-tendon Modeling Framework to Evaluate Muscle-level Performance of Ankle Exoskeletons during Human Walking

by
Nabil Salih Khan

A thesis submitted to the Graduate Faculty of
North Carolina State University
in partial fulfillment of the
requirements for the Degree of
Master of Science

Biomedical Engineering

Raleigh, North Carolina

2013

APPROVED BY:

Dr. Richard Goldberg	Dr. Michael Lewek

Dr. Gregory Sawicki
Chair of Advisory Committee

DEDICATION

بِسْمِ ٱللَّهِ ٱلرَّحْمَٰنِ ٱلرَّحِيمِ

(In the name of God, the Compassionate, the Caring)

To my parents - whose guidance, persistance, and support are responsible for any and all accomplishments in my past, present, and future.

BIOGRAPHY

The author was born of two parents of Bangladeshi decent in the honorable town of Hunstville, Alabama. His present whereabouts are in the Triangle of North Carolina.

ACKNOWLEDGEMENTS

I would like to thank my research advisor for spending numerous hours on tedious editing for days (and nights) on end to help transform my soulless prattling into thoughtful and engaged writing. Without his exceptional patience in responding to painfully similar and repetitive questions, I would not have developed an aptitude in muscle-tendon dynamics or honed an ability to interrogate and interpret scientific works. Hopefully both of these features are reflected in this document.

I additionally owe a great deal to my masters committee - not only were the members willing to join under a markedly short and unorthodox notice, but were also willing to countenance and accommodate delay after delay, despite the inconvenient impact on their summer schedules.

I would be remiss not to acknowledge the Department of Biomedical Engineering at both UNC and NCSU here - especially the administrative staff. Without their help trudging through the bureaucracy of two dissimilar graduate schools, I would not have been able to supplement my graduate education with the formative classes I had the good fortune of taking.

Finally, I would like to thank my wife for ensuring that I was fed and looked after throughout this whole ordeal - even when I was far too sleep-deprived and odorous to merit such endearing care. Hopefully, by the time this is finalized, I will have found gainful employment and, in doing so, justified the investment of your time and effort. You are very good to me.

TABLE OF CONTENTS

LIST OF TABLES

LIST OF FIGURES

Chapter 1

Why Model Wearable Exoskeletons?

Mapping Morphology to Performance The composition, behavior, and interactions between a system's components often dictate the emergent behaviors and capabilities of the system as a whole. This dictum has motivated the reductionist approach to modern scientific inquiry in a multitude of fields; the field of human locomotion is no different. Decades of research have been invested in characterizing the critical mechanisms that facilitate locomotion, as well as patterns and features indicative of a healthy locomotion system. Through studies that have deconstructed muscle and tendon architecture[64], muscle/tendon force production[47][67], and movement related energy consumption[2], many of the parameters (collectively referred to as *morphology*) that govern these mechanisms have been identified. Coupled with research that has established estimates of healthy *performance* for human locomotion such as walking kinetics[37][59](i.e. forces and moments), kinematics[59](i.e. positions, velocities, and accelerations), and resultant mechanical and metabolic work, a more holistic understanding of human locomotion has come to fruition. However, the explicit effect of morphology on resultant human locomotion performance remains unclear.

This missing relationship has a profound effect on the ability to efficiently design and develop lower-limb assistive devices; most prominently, the development of wearable exoskeletons. Ranging in form factor from passive ankle orthoses that rely on compliant materials to modify movement patterns, to fully powered whole leg exoskeletons capable of high mechanical output, these devices hold considerable promise in the fields of human gait rehabilitation and augmentation. Of particular interest are wearable exoskeletons designed to assist the ankle joint, due of the ankle's role as the primary relative power producer during human walking[24]. While prosthetics can internally function as "black boxes" and can achieve the desired locomotive output through any means necessary, wearable exoskeletons are not afforded such flexible design constraints. Achieving a certain set of performance specifications with a wearable exoskeleton is contingent upon synergistically interacting with the existing biological locomotive systems.

Without understanding the necessary internal interactions that cascade from the existing morphology, wearable exoskeletons can not be intelligently customized to effectively rehabilitate or augment.

Unfortunately, current technology prohibits the safe manipulation of living biological morphology to investigate resultant performance. However, computational modeling offers a powerful framework in which morphology might be varied and mapped to performance outcomes. By utilizing models based on experimentally established morphology values and subsystem behaviors, parameters can be altered and probed at various levels of system integration to determine how performance emerge from morphology. Moreover, the model framework can be easily configured to simulate a wearable exoskeletons interaction with the biological system based on it's own morphology parameters (passive stiffness, exoskeleton geometry, etc).; this proffers a cost and time effective method of prototyping exoskeletons for design optimization. Especially since recent iterations of exoskeletons targeting the human ankle have drawn inspiration from biological mechanisms of the human-ankle-foot system, it is imperative to have a data-driven modeling framework that can verify that existing biological systems are indeed the benchmark to aim towards. Armed with this knowledge, the interaction that an exoskeleton has with the underlying physiology of the human wearer can be better understood and favorably manipulated to more efficiently assist human locomotion.

Whether operating in a biological system such as the human lower leg, or an artificial system like a wearable exoskeleton, the system's morphology will ultimately dictate performance. Through the development of a data-driven computational framework, many issues that impact exoskeleton design could be addressed. Firstly, a flexible system in which morphology can efficiently be manipulated would elucidate whether exoskeletons *should* take inspiration from human morphology, or whether there are more optimal ways of achieving important performance outcomes (such as reduced metabolic costs for locomotion). Secondly, artificial morphologies of an exoskeleton might be varied and interfaced with a biological morphology model to determine both a) how best to configure exoskeletal morphology to optimize performance; and b) how the internal biological structures are impacted when such an intervention has taken place. Not only does a robust computational framework avert incurring significant costs from prototyping wearable exoskeletons, but such a novel data-driven approach might be further developed to address both unassisted and assisted muscle-tendon dynamics in a multitude of conditions. Various gait patterns (e.g. level and graded hopping and running), altered MTU morphologies following neurological or musculoskeletal injury, and combinations of the gait patterns and morphology deficits could be quickly integrated and studied. Hopefully, such inquiry can manifest in carefully informed designs and efficient advances in the clinical and applied sciences that might benefit many to come.

Chapter 2

Modeling the Interplay between Plantar Flexor Muscle-tendon Morphology, Neuromechanics, and Energetics during Human Walking

2.1 Introduction

Muscle-tendon morphology varies greatly across the human lower-limb, but an understanding of the relationship between morphology and function during human locomotion is limited. This study defines muscle-tendon unit (MTU) morphology as the set of parameters that describe the dimensions and material properties of the muscle contractile element (CE) (i.e. fascicles and parallel connective tissues) and in series elastic tissues (SEE) (i.e. tendon, aponeurosis). This includes total muscle-tendon length (L_{MTU_0}), relative muscle length ratio ($^{L_{CE}}/_{L_{MTU}}$), muscle physiological cross-sectional area (PSCA), muscle pennation angle, and tendon stiffness (K_t). In the human lower-limb, MTU morphology follows a proximal to distal gradient. Proximal MTUs tend to have longer lengths, higher relative muscle length ratios, larger muscle physiological cross sectional areas, smaller muscle pennation angles, and shorter, stiffer series tendons than distal MTUs[3][64][65].

MTU morphology in the lower-limb may organize according to specific locomotor functional sub-tasks[3][9][17]. It has been suggested that the bulky and stiff architecture of proximal MTUs may be suited to producing mechanical power/work and high fidelity position control of a joint, whereas the streamlined, compliant architecture of distal MTUs may be more suited for economical force production and shock absorption at the interface with the ground[9][17]. The

potential for MTU architecture to drive specialization in performance that organizes across the lower-limb is clear; however, the challenge of making simultaneous measures of mechanics and energetics of individual MTUs *in vivo* has made it difficult to link MTU structure and function in the context of human locomotion - especially with regard to metabolic energy cost[63].

Compliant muscle-tendon architecture enables a number of elastic mechanisms that can improve locomotion performance. These mechanisms include power amplification, power attenuation and energy conservation via elastic energy storage and return[3][57]. For example, the human ankle plantar flexors have short, pennate muscle fascicles and a long series elastic tendon (i.e. the 'Achilles') that allow them to produce large amounts of mechanical power[24] with high mechanical efficiency[37][47][60]. In the major plantarflexors (i.e.the soleus (SOL), lateral gastrocnemius (LG), and medial gastrocnemius (MG) - all collectively referred to as the triceps surae), series elastic tissues comprise more than 80% of the total MTU length[64]. Tendonous tissues behave similar to mechanical springs, and will undergo stretch that is load dependent. Stretch in series elastic tissues effectively act to decouple muscle fascicle excursions from the movement of the attached limb[54][56]. The decoupling of CE and SEE in the triceps surae MTUs is extensive during the stance phase of human walking, with more than half of the MTU excursion being taken up in stretching series elastic tissues[22][27][39][45].

The decoupling effect afforded by compliant muscle-tendon architecture is an integral feature for limiting the metabolic energy consumed by the triceps surae muscles during human locomotion[54][56]. Many studies have demonstrated that the Achilles tendon undergoes a spring-like energy storage and return cycle (i.e. catapult action) during human walking[22][27][39][45]. These same studies all confirm that the triceps surae muscle fascicles all operate at relatively slow shortening velocities. Metabolic energy consumed by a muscle is directly related to its shortening velocity during movement with faster contractions costing much more than slower ones[35]. Thus, significant stretch in tendonous tissues during the stance phase of walking improves metabolic economy of force production by limiting the length changes and velocities in muscle fascicles. Furthermore, a recent study indicates that soleus fascicles operate on the ascending limb and plateau portion of its force-length curve[58], an operating point that is favorable for muscle force production/unit activation, which is a factor that could also limit metabolic energy expenditure. Ultrasound imaging experiments provide strong evidence for an energy saving elastic mechanism in the human plantarflexors during walking. Because it is impossible to non-invasively manipulate MTU architecture *in vivo*, it is difficult to observe how specific morphological features of the plantarflexors (e.g. Achilles tendon stiffness) might influence energy savings along the continuum of compliant architectures.

Unlike experimental studies, which are limited to observing existing behavior in biological systems, modeling studies are able to selectively deviate from biological constraints to predict how morphology drives mechanical[5][6] and metabolic performance[43][47]. For example,

Lichtwark et al. combined a Hill-type muscle model and empirical measurements of walking kinematics and kinetics with an empirical estimate of medial gastrocnemius (MG) series elastic stiffness to ask: is the Achilles tendon stiffness optimized to maximize MG mechanical efficiency for both walking and running? The conclusions suggested that Achilles tendon stiffness may be tuned to efficiently modulate the MG during walking more than running. Other computer models have more comprehensively incorporated experimental measures important to gait dynamics to determine whether human leg muscle morphology enables metabolic optimality. Krishnaswamy et al. used empirically measured values for the kinetics, kinematics, and neural control parameters of walking to discover the morphological features of the triceps surae muscles that both minimized metabolic energy expenditure and recovered normal ankle joint moments with small error (i.e. a pareto optimal solution) [43]. Krishnaswamy et al. demonstrated strong evidence that human ankle plantarflexors may have MTU architecure tuned for metabolic energy minimization, but they presented limited information on the relative importance of specific morphological features (e.g. MTU slack length vs. muscle length ratio vs. series tendon stiffness) to overall performance.

The aim of this study was to use a simple, data-driven modeling framework to examine the influence of MTU morphology on the muscle-tendon interaction dynamics, neural control requirements and metabolic energy cost of the ankle plantarflexors during human walking. We hypothesized that for MTU morphologies capable of producing human-like ankle moment patterns, metabolic energy expenditure would systematically decrease with increasing MTU compliance. We based our hypothesis on the idea that increasing compliance should allow more extensive decoupling between MTU and muscle fascicles and enable force-length and force velocity operating points favorable for metabolic economy. To address the hypothesis, we constructed a simplified model of the human triceps surae group using a single, lumped, uniarticular ankle plantarflexor MTU. The lumped MTU had muscle force generating capacity of the combined triceps surae group and incorporated a muscle force-length relationship based on recent ultrasound studies[58] as well as geometry and attachments consistent with the latest MRI muscle architecture data for the soleus[64]. Using the model, and an inverse approach, we could input experimental values for the ankle angle and soleus fascicle (CE) strain pattern[58] from human walking at preferred speed and then estimate the length changes of the MTU and the SEE as well as the required muscle forces, muscle activation pattern and metabolic power output for any given ankle MTU morphology. We explored a morphology parameter space defined by numerous combinations of (1) overall MTU length (L_{MTU_0}) (2) the ratio of CE length to overall MTU length ($^{L_{CE}}/_{L_{MTU}}$) and (3) the linear series elastic tissue (SEE) stiffness (K_t). In this framework, the most compliant MTU morphologies would have a low $^{L_{CE}}/_{L_{MTU}}$ ratio and a lowK_t. By examining the metabolic cost of each of the ankle MTU morphologies in this parameter space we could ask: What are the morphological features that generate human-

like ankle joint moment at the lowest metabolic cost during walking at 1.25 ms^{-1}?

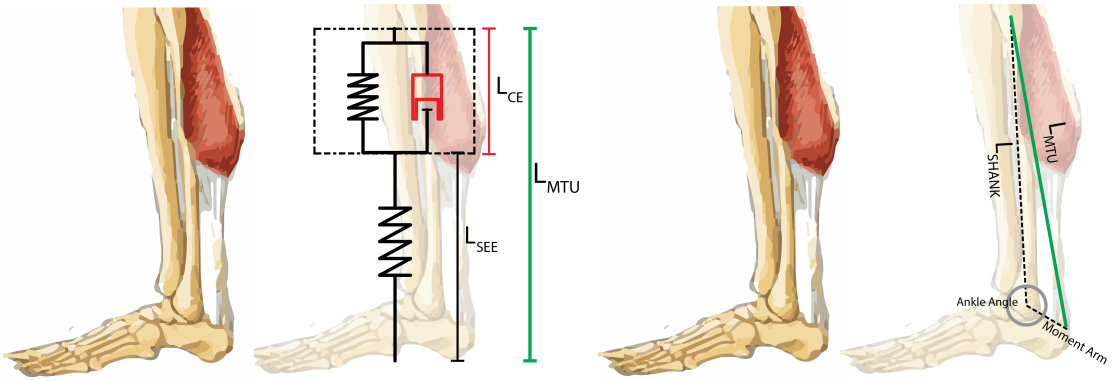

(a) (b)

Figure 2.1: **Schematic of MTU Components.** a) The MTU was comprised of a single CE and SEE which represented all muscle fasciles and connective tissues in the MG, LG, and SOL muscles. b) The MTU originated 12.5% distally from the tibial condyles and inserted into the calcaneal tuberosity. Details are developed in Appendix A.1.

2.2 Methods

2.2.1 Experimental Data

The kinetics and kinematics data utilized in this model were taken from previously published studies[58][59]. Ankle angle data were collected via motion analysis techniques, and averaged across 9 healthy subjects (N=9; 5 males, 4 females; mass=80.3$\pm$14.7 kg; height=170$\pm$3 cm; leg length=92$\pm$2 cm)[59] walking on a motorized treadmill at 1.25 ms^{-1}(Figure 2.2a, Figure 2.2b). Ground reaction forces were captured by force platforms for each foot during the stance phases and combined with foot segment inertial estimates to calculate ankle joint moments, which were then normalized by subject mass and averaged.

The CE strain profile data, presented by Rubenson et al., were collected from the right solei of 8 healthy participants walking on a motorized treadmill at 1.20 ms^{-1}using ultrasound techniques(Figure 2.2c). Optimal fascicle lengths L_{CE_0} were experimentally calculated for each subject using passive and active force-length curves measured with a dynamometer in conjunction with ultrasound techniques, and used to normalize the CE length profile data before averaging[58].

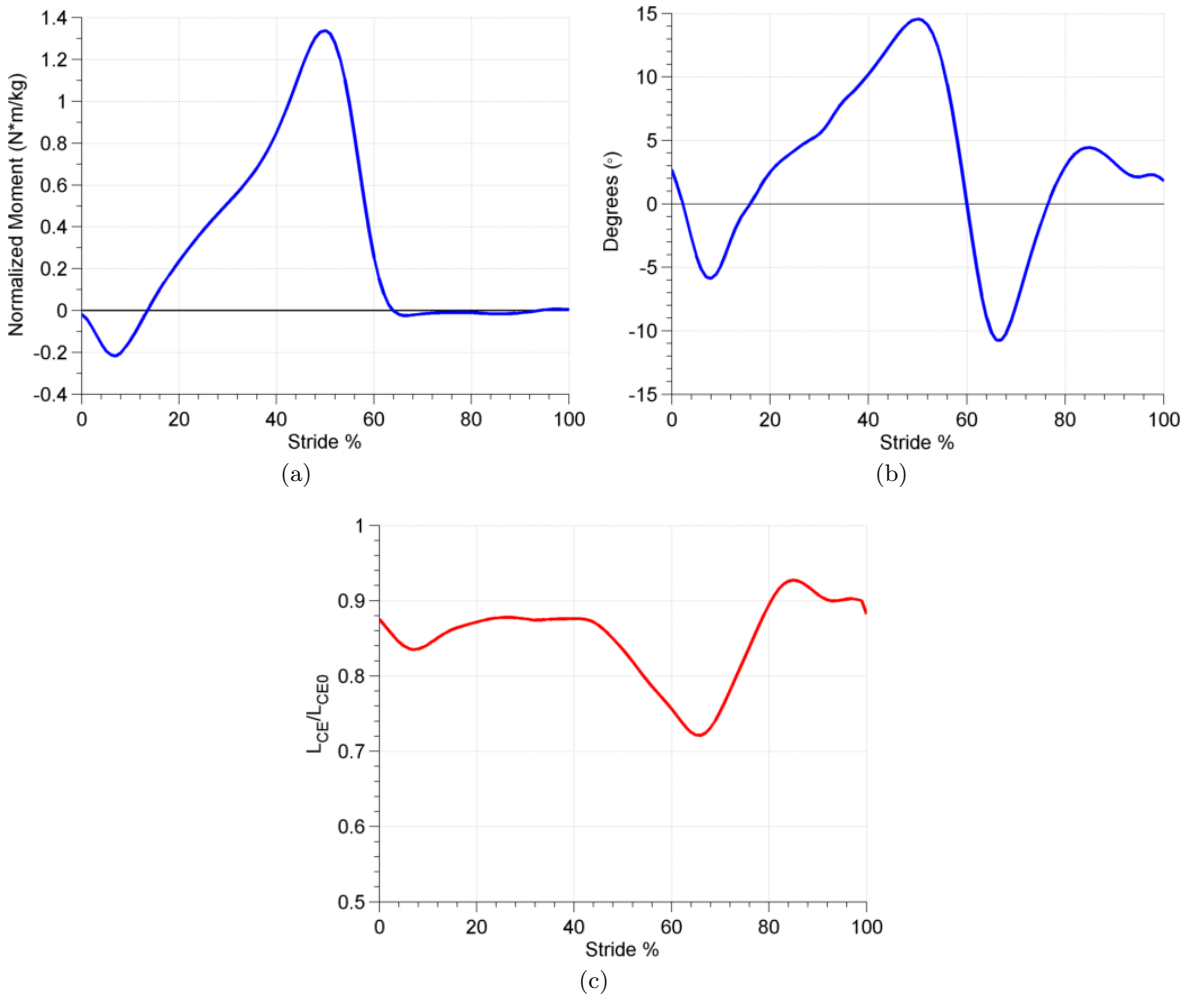

Figure 2.2: **Experimental time-series inputs.** a) Moment profile and b) corresponding ankle angle for walking at 1.25 ms^{-1} (N=9; 5 males, 4 females; mass=80.3±14.7 kg; height=170±3 cm; leg length=92 ± 2 cm)[59]. b)Positive ankle angles indicate dorsiflexion and negative ankle angles indicate plantar flexion. c) Length profile of soleus muscle normalized to L_{CE_0} while walking at 1.20 ms^{-1}(N=8; 8M; age=26 ± 3.51 years; mass=70.31 ± 9.18 kg)[58].

2.2.2 Components of MTU Model

Our study used a consolidated Hill-type muscle model to represent the SOL, MG, and LG[67]. The model consists of a simplified muscle tendon unit (MTU) made up of a series elastic element (SEE), a contractile element (CE), and a passive elastic element (PEE) acting in parallel with the CE. The muscle body of a given muscle is represented by the CE and PEE in parallel. The CE represents the unidirectional actuation and force production exhibited by a muscle fascicle when activated, while the PEE models the muscle elasticity stemming from internal connective tissue and energy stored in cross-bridges[67]. The SEE respresents all cumulative connective tissue in series with a fascicle between the origin and insertion of a given muscle. This includes tendon attachements, free tendons, and aponeuroses. Each element has the ability to generate and maintain force.

CE Dynamics. CE force generation is modeled in accordance with Hill-type contraction dynamics[67]. In this framework, the CE force F_{CE}, is related to maximum CE force capacity $F_{CE_{MAX}}$, activation signal α, CE length L_{CE}, and CE velocity V_{CE} (Eq. 2.1). Activation signal α is normalized to the maximum magnitude of activation that a muscle can be activated. $F_{CE_{MAX}}$ is the maximum force a muscle is capable of generating while being held isometrically. The length at which this maximum is achieved, L_{CE_0}, is consequently used to normalize the CE length ($\widetilde{L_{CE}}$). $V_{CE_{MAX}}$, the shortening velocity at which the CE can no longer produce a measureable force, is used to normalize V_{CE}, which is represented as $\widetilde{V_{CE}}$.

$$F_{CE} = F_{CE_{MAX}} * (\alpha(t) * f_{\widetilde{L_{CE}}(t)^{Active}} * f_{\widetilde{V_{CE}}(t)} + f_{\widetilde{L_{CE}}(t)^{Passive}}) \tag{2.1}$$

The functions $f_{\widetilde{L_{CE}}^{Active}}$, $f_{\widetilde{L_{CE}}^{Passive}}$, and $f_{\widetilde{V_{CE}}}$ characterize the normalized force-length (F-L) and force-velocity (F-V) relationships described by Zajac[67]. $f_{\widetilde{L_{CE}}^{Active}}$, or the active portion of the F-L curve, is defined in Eq. 2.2 and shown in Figure 2.3a. Regions of the F-L curve are defined as the steep ascending limb ($\widetilde{L_{CE}} < 0.75$), shallow ascending limb ($0.75 < \widetilde{L_{CE}} <$ .95), plateau region ($0.95 < \widetilde{L_{CE}} < 1.05$), and descending limb ($1.05 < \widetilde{L_{CE}}$) per convention established by Arnold and Delp[5]. $f_{\widetilde{L_{CE}}^{Passive}}$, or the passive portion of the F-L curve, is defined in Eq. 2.3 and plotted in Figure 2.3a. Unlike the active portion of the F-L curve, which is scaled by the activation of the muscle body and contributes significantly throughout the range of $\widetilde{L_{CE}}$, the passive contribution relies on the $F_{CE_{MAX}}$ characteristics of the CE alone, and only begins to influence F_{CE} generation when $\widetilde{L_{CE}} < 1.0$. Equation constants for Eq. 2.2 and Eq. 2.3 were taken from Rubenson et al.[58].

$$f(\widetilde{L_{CE}}_{active}) = e^{-|\frac{\widetilde{L_{CE}}^{b}-1}{s}|^{a}} \tag{2.2}$$

$$f(\widetilde{L_{CE_{passive}}}) = a * e^{b(\widetilde{L_{CE}}-1)} \tag{2.3}$$

$f_{\widetilde{V_{CE}}}$, or the F-V curve, is defined by Eq. 2.5 and Eq. 2.6[2]. For our study, L_{CE} shortening is defined as a positive V_{CE}, while L_{CE} lengthening is defined as a negative V_{CE}. The F-V curve is plotted in Figure 2.3b.

$$V_{CE} = -\frac{\Delta L_{CE}}{\Delta t} \tag{2.4}$$

$$f(\widetilde{V_{CE_+}}) = \frac{1 - \widetilde{V_{CE}}}{1 + \frac{V_{CE}}{GV_{MAX}}} \tag{2.5}$$

$$f(\widetilde{V_{CE_-}}) = 1.8 - .8\frac{1 + \widetilde{V_{CE}}}{1 - 7.56\frac{V_{CE}}{GV_{MAX}}} \tag{2.6}$$

SEE Dynamics. SEE force generation is modeled with a non-linear F-L relationship. This nonlinearity exists at low forces in comparison to the connected muscle capability, which is exhibited by biological connective tissues and is referred to as a "toe region" [47][67]. Though connective tissue strain patterns suggest a linear force length relationship in moderate to high forces, a non-linear model more accurately represents the requisite elastic tissue excursion to achieve such forces. Instantaneous stiffness K_{SEE} was modeled as a function of $F_{CE_{MAX}}$ and a linear tendon stiffness K_t, as seen in Eq. 2.7[47]. To determine the force length pattern for a given $F_{CE_{MAX}}$ and K_t, the instantaneous stiffness K_{SEE} was integrated across the range of forces to determine dL_{SEE} (Eq. 2.8). The inverse of this result was then used to map F_{SEE} to a given L_{SEE}. The SEE could only store and return energy for L_{SEE} values above L_{SEE_0}.

$$K_{SEE} = K_t(1 + \frac{.9}{-e^{\frac{Q*F_{CE}}{F_{MAX}}}}) \tag{2.7}$$

$$dL_{SEE}(F_{CE}) = \int_{F_{CE}=0}^{F_{CE}=F_{MAX}} \frac{dF_{CE}}{K_{SEE}(F_{CE})} \tag{2.8}$$

2.2.3 Parameter Values

A recent muscle architecture study was consulted to determine MTU architecture and joint geometry values for the lumped model[64]. Ward et al. implemented careful dissection and MRI techniques on 21 cadavers (N=21; 9 males, 12 female; Age=83±9 years; height=168.4±9.3 cm; weight=82.7±15.3 kg) to comprehensively quantify average skeletal lengths, muscle body length, muscle fascicle length, pennation angles, and physiological cross-sectional areas(PCSA) of lower limb muscle bodies. Elastic features beyond the muscle bodies, such as external tendons and

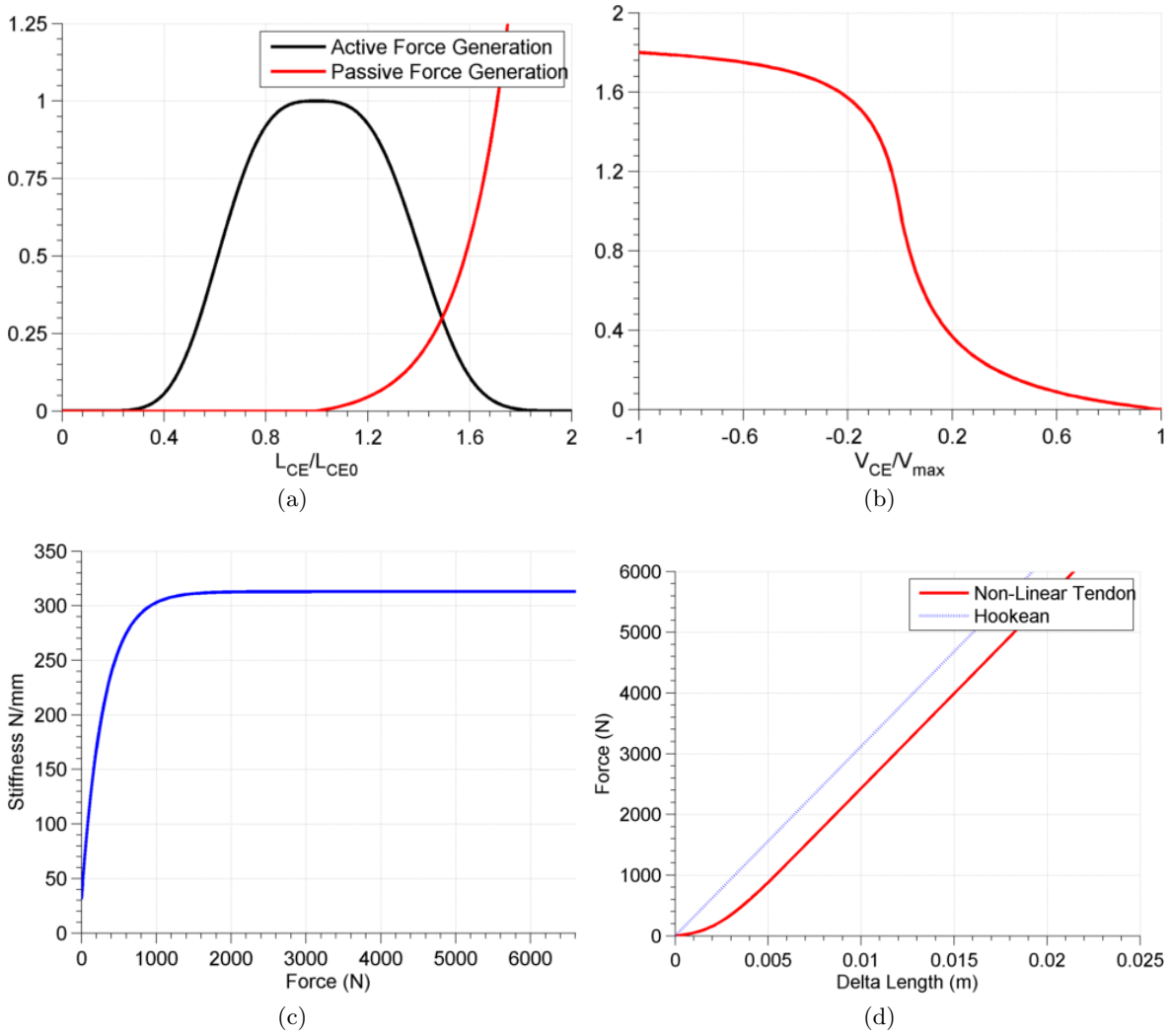

Figure 2.3: **Force characteristics of model elements.**a) Zajac parameterization of active and passive Force-Length CE characteristics; Model coefficients taken from Rubenson[58]. b) Zajac parameterization of Force-Velocity characterstics[67]. c) Force - Stiffness relationship for non-linear SEE. Steady state stiffness $K_t = 313.0\ Nmm^{-1}$. d) Resultant force length characteristic of SEE ($K_t = 313$ Nmm^{-1}, $F_{CE_{MAX}} = 6000$ N; red solid) compared to hookean force-length representation ($K_t = 313.0$ Nmm^{-1}; blue dashed).

tendinous attachments, were not reported and were excised prior to muscle body measurement. Arnold and Delp used Ward's skeletal and muscle body data and extrapolated elastic tissue lengths to fit origin and insertions of the respective muscles[7]. Average muscle fascicle lengths from Ward were divided by the total muscle-tendon slack length estimations presented in Arnold and Delp for the triceps surae group, and then averaged according to their respective PCSAs to determine the weight averaged percentage of muscle to muscle-tendon unit for the tricep surae ($^{L_{CE}}/_{L_{MTU}}$). A weighted average according to PCSA was also used to determine lump pennation angle. The resultant muscle to muscle-tendon percentage was then multiplied by the cosine of the pennation angle to yield a lump $^{L_{CE}}/_{L_{MTU}}$ ratio of 10.8%. $F_{CE_{MAX}}$ was approximated at 6000 N, which compares favorably with model estimaes for the sum of the tricep surae[7][43][46]. $V_{CE_{MAX}}$ for the lump model was defined using a weighted average via Ward et al. reported PCSAs of $V_{CE_{MAX}}$ values for the SOL and GAS reported by Geyer et al.[29]. This calculation yielded a normalized $V_{CE_{MAX}}$ of $8.24 * L_{CE_0}$ ms^{-1}.

A novel geometric framework was developed to house the lumped model. Though the triceps surae include both biarticular(MG, LG) and uniarticular(SOL) muscles, a uniarticular configuration was chosen for the lumped model. The model subject of our study was assigned a height of 170 cm and a weight of 70 kg. The length of the lower limb segment, known as the shank and defined by the vector intersecting the lateral and medial femoral condyles to the vector intersecting lateral and medial maleoli of the ankles, was approximated to be 3 cm greater than the reported length of the tibia in Ward et al. (37.0±2.2 cm) to comfortably accomodate the femoral condyle[64]. The lump model MTU originated 12.5% from the top of the shank and inserted into the calcaneal tuberosity. Additional detail concerning lump MTU origin/insertion architecture, a comparison of moment arms between lump MTU and individual triceps surae muscles, as well as a comparison of lump and individual muscle length models can be found in Appendix A.1.

2.2.4 Model Framework

A morphology vector $\vec{M}$ was defined with a L_{MTU_0}, $^{L_{CE}}/_{L_{MTU}}$, and K_t. The ankle angle from Sawicki et al.[59] was applied to the joint geometry to determine L_{MTU}, the distance between the insertion and origin of the MTU for each data point of the stride profile. Since the MTU consists of the CE and SEE in series configuration,

$$L_{MTU}(t) = L_{SEE}(t) + L_{CE}(t) \tag{2.9}$$

holds true for all L_{MTU}'s. L_{CE_0} was determined by applying the $^{L_{CE}}/_{L_{MTU}}$ element of $\vec{M}$ to L_{MTU_0}. Per Eq. 2.9, a L_{SEE_0} was concurrently defined.

The normalized L_{CE} strain pattern from Rubenson[58] was then multiplied to the L_{CE} to

determine each CE length for each point during the stride. Then, using Eq. 2.9, the L_{SEE} for all time points was determined. The SEE force-dynamics described in Eq. 2.8 were utilized to calculate the F_{SEE} at each L_{SEE}. Since the CE and SEE are in series, it was assumed that

$$F_{CE}(t) = F_{SEE}(t) = F_{MTU}(t) \tag{2.10}$$

for all time points in the stride.

2.2.5 Assessment Metrics

The F_{MTU} was applied across the moment arm for each point in the stride to determine the triceps surae plantar flexor moment $m_{model_{PF}}$. The net moment profile data from Sawicki et al.[59] normalized to a model subject mass of 70 kg, m_{net}, was used as a comparison to $m_{model_{PF}}(\vec{M})$ (Figure 2.2a). The F_{CE} and V_{CE} were used to calculate the average work performed by the CE across the stride. Finally, F_{CE}, V_{CE}, and L_{CE} were input into Eq. 2.1 to back calculate the necessary activation, with which the metabolic power and total metabolic cost were calculated.

Moment RMSE. The $m_{model}(\vec{M})$ was assessed against the net ankle moment profile data m_{net} by calculating a conditional root mean square error, or RMSE (Eq. 2.11). Because the tricep surae can only produce moments in the plantar flexion direction, RMSE was calculated where the m_{net} was greater than 0 N-m. Furthermore, the RMSE was artifically inflated by 5 N-m for each time point for which the $m_{model_{PF}}(\vec{M})$ was less than m_{net} between the time points t= 35 and t=50 to penalize underestimating the plantar flexor moment in the 35 - 50% portion of the stride. The justification for this range developed in Appendix A.2.

$$RMSE = \sqrt{\frac{\sum^{n}(m_{model_{PF}}(\vec{M})(t) - m_{net}(t))^2}{n}} \tag{2.11}$$

Mechanical power. The mechanical power for each point was calculated across the stride. For a given element, mechanical power is calculated via the following equation:

$$P_{Mech}(t) = F_{Element}(t) * V_{Element}(t) \tag{2.12}$$

The average positive mechanical work performed by an element was also calculated. For every $P_{Mech} > 0$,

$$W^{+}_{Mech} = P_{Mech}(t) * \Delta t \tag{2.13}$$

Table 2.1: **Equation Coefficients and Sources.**

Equation	Coefficients	Source
Eq. 2.2	a=3.188; b=.8698; s=.3914	[58]
Eq. 2.3	a=2.38e-2; b=5.31	[58]
Eq. 2.5, Eq. 2.6	G=.17	[2]
Eq. 2.7	Q=20	[47]

Metabolic cost estimate. A metabolic cost estimate model was used to estimate the energy expenditure by the lumped muscle during the gait[2]. The heats for all states of the muscle, including maintanence, shortening, resting, and activation, are encapsulated and represented in this calculation. The metabolic power consumed for any given time is:

$$P_{met}(t) = \alpha(t) * F_{CE_{MAX}} * V_{CE_{MAX}} * f_{met}(\widetilde{V_{CE}}(t)). \tag{2.14}$$

$f_{met}(\widetilde{V_{CE}})$ represents empirically based heat measures that have been related to muscle velocity[2] (Eq. 2.15, Eq. 2.16).

$$f_{met}(\widetilde{V_{CE}}) = .23 - .16e^{-8\widetilde{V_{CE}}};\ \widetilde{V_{CE}} > 0 \tag{2.15}$$

$$f_{met}(\widetilde{V_{CE}}) = .01 - .11\widetilde{V_{CE}} + .06e^{23\widetilde{V_{CE}}};\ \widetilde{V_{CE}} < 0 \tag{2.16}$$

Total metabolic work expended over a stride was calculated by summing the product of each metabolic power measurement and the time between data points over the given time interval:

$$W_{met} = \sum (P_{met}(t) * \Delta t) \tag{2.17}$$

MTU Compliance To assess overall compliance of a given MTU morphology, the 'fixed-end compliance', or FEC, was calculated. FEC refers to the amount of strain that a muscle fascicle would undergo in a maximal 'fixed-end' contraction as it shortens against the stretch of its series tendon[56]. ${}^{L_{CE}}/_{L_{MTU}}$ is multiplied by L_{MTU_0} to determine the lengths of the CE and SEE elements. The CE is maximally activated against the SEE with a stiffness of K_t, and the strain value of the CE at which CE and SEE force generations are equal (Eq. 2.10) is the FEC. An FEC of 0 indicates that the MTU has no compliance, whereas an FEC of 1 incidaces an MTU with infinite compliance.

2.2.6 Model Implementation

Finding the $\vec{M}_{bio}$ solution. Using the framework described above, the vector that minimized the RMSE between $m_{model_{PF}}(\vec{M})$ and m_{net} while maintaining the ${}^{L_{CE}}/_{L_{MTU}} BIO$ of 10.8%

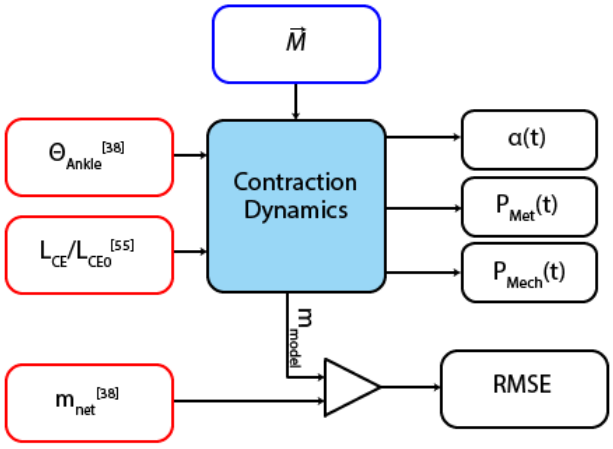

Figure 2.4: **Simplified block diagram of simulation inputs and outputs.** Variable input $\tilde{\mathbf{M}}$ is outlined in blue. Experimental profiles are outlined in red, and calculated outputs are outlined in black.

(Section 2.2.3), was calculated using the `fminsearch` MATLAB function. The `fminsearch` function performs an unconstrained nonlinear optimization using the Nedler-Mead Simplex method [44]. This morphology vector was defined as the 'human' $\vec{M}_{bio}$ configuration. The L_{MTU_0} of the $\vec{M}_{bio}$ solution vector was then held constant, and a contour graph mapping the RMSE and Metabolic cost of the surroundingt K_t and $^{L_{CE}}/_{L_{MTU}}$ space were plotted (Figure 2.5, Figure 2.7). The orthogonal contour plane varying L_{MTU_0} and K_t can be found in Appendix A.3.

Absolute minimum. An unconstrained `fminsearch` was performed across all elements of the morphology vector to determine the absolute minimum RMSE of the vector space, $\vec{M}_{abs}$. Then, the L_{MTU_0} for $\vec{M}_{abs}$ was held constant and a contour graph of the RMSE and metabolic cost of the surrounding elements could be generated.

FEC and $\mathbf{W_{met}}$ Lastly, a volume of solutions between $\vec{M}_{bio}$ L_{MTU_0} and $\vec{M}_{abs}$ L_{MTU_0} were sampled and filtered according to the criterion RMSE($\vec{M}$) $\leq$ RMSE($\vec{M}_{bio}$). The FEC and metabolic cost W_{met} were then calculated for each morphology vector and plotted in Figure 2.9.

2.3 Results

Features of human-like morphology contour graphs The $\vec{M}_{bio}$ search (Section 2.2.6) resulted in the solution vector $\vec{M}_{bio}$ = [.366 m, .108, 315.4 Nmm^{-1}]. Figure 2.5a displays a

Table 2.2: **Model Parameter and Input Values.**

Parameter	Units	Value	Source	Details
Mass	kg	70	[64]	Within 1 SD of Ward et al.(82.7 ± 15.2)
Height	m	1.70	[64]	Within 1 SD of Ward et al. (168.4 ± 9.3 cm)
Shank Length	m	.40	[64]	.03 m above tibial length reported by Ward et al. (37.1 ± 2.2) to capture distance to femoral condyles.
$\vec{\mathbf{M}}_{bio}$ $^{L_{CE}}/_{L_{MTU}}$	N/A	.108	[7][64]	Fasicle lengths of SOL, MG, and LG reported by Ward et al. respectively divided by sum of Ward et al. fasicle length and Arnold et al. connective tissue lengths, and scaled according to PCSA reported in Ward et al.
$\mathbf{F_{CE_{MAX}}}$	N	6000	[7]	Similar to triceps surae approximation (5500.3 N) by Arnold et al., based on PCSA of Ward et al. 2010 data.
$\mathbf{V_{CE_{MAX}}}$	ms^{-1}	$8.24 \times L_{CE_0}$	[29][64]	SOL and GAS reported by Geyer et al. and scaled based on PCSA of Ward et al. 2010 data.

sample of model solutions that reside on the $^{L_{CE}}/_{L_{MTU}} = .366$ m plane. A singular minimum RMSE point of the contour exists at $\vec{M}_{bio} = [.108, 315.4\ \text{Nmm}^{-1}]$, with an RMSE value of 10.7 N-m. The blank region in the top right of the graph denotes where the morphology vectors produced an $m_{model_{PF}}(\vec{M})$ that exceeded the capabilities of the CE and SEE parameters. A steep cliff-like set of solutions exists underneath the vector band that where the $m_{model_{PF}}(\vec{M})$ begins to drop below m_{net} between the 35% to 50% of the stride and are artificially penalized beyond the calculated RMSE (Section 2.2.5).

The metabolic costs associated with the morphology vectors in Figure 2.5a are plotted in Figure 2.5b. Again, because the capabilities of the governing element parameters were exceeded in the top right, no metabolic cost could be calculated. Unlike the RMSE plot in Figure 2.5a, where the contour featured an assymetric valley of close to optimal solutions, the metabolic cost contour was a steady declining gradient as the percentage of CE in the MTU decreased.

$\vec{M}_{bio}$ behavior. The behaviors of the $\vec{M}_{bio}$ MTU model is illustrated in Figure 2.6. The moment generated by the $\vec{M}_{bio}$ solution had as RMSE of 10.7 N-m. This solution exceeded the peak moment of m_{net} of 93.7 N-m by 15.1 N-m at $m_{model_{PF}}(\vec{M}) = 108.8$ N-m. The solution vector also produced ample moment during the swing phase of the stride (Figure 2.6a). The activation

profile necessary to produce the F_{CE} peaked at 95.3% of maximum activation (Figure 2.6c). There was significant coactivation during prior to heel strike and during the swing phase. The CE performed 13.6 J of positive mechanical work during the gait (Figure 2.6d). The strain of the lumped SEE did not exceed 104% of L_{SEE_0} (Figure 2.6e). The metabolic power peaked at 283 W, with a total metabolic cost of 50.3 J (Figure 2.6f).

Features of absolute minimum contour graphs. The $\vec{M}_{abs}$ search (Section 2.2.6) resolved at morphology solution $\vec{M}_{abs}$ = [.363 m, .0367, 341.5 Nmm^{-1}]. The contours planes containing $\vec{M}_{abs}$, shown in Figure 2.7, share the same general features of the RMSE and metabolic cost contours of the $\vec{M}_{bio}$. A blank space on the contours persists due to the morphology vector solutions exceeding the capabilities of the element parameters (Figure 2.7). The shape of the contour remains similar to Figure 2.5a and Figure 2.5b; however, the entire cross-section is translated towards the origin.

The metabolic cost of the $\vec{M}_{abs}$ plane also resolved similarly to the $\vec{M}_{bio}$ plane. Once again, the contour takes the form of a steadily declining gradient, with the lowest metabolic costs (W_{met} = 0 J) residing at the $^{L_{CE}}/_{L_{MTU}} = 0$ plane, where there is no muscle to activate and create an enegy expenditure.

$\vec{M}_{abs}$ **behavior.** The characteristics of the MTU with $\vec{M}_{abs}$ are shown in Figure 2.8. The moment profile generated by the $\vec{M}_{abs}$ solution had an RMSE of 6.21 N-m, and had a peak-to-peak difference from m_{net} of +2.3 N-m. Again, there was significant coactivation prior to heel strike and during the swing phase. The requisite profile necessary to produce the forces via CE lengths presented in Rubenson et al.[58] peaked at 56% of maximum activation. Absolute length changes and element strains of $\vec{M}_{abs}$ are displayed in Figure 2.8b and Figure 2.8e. Figure 2.8d displays the mechanical power produced by each element; the average positive CE work done across the stride was 3.71 J. Lastly, the total metabolic cost for $\vec{M}_{abs}$ was 14.2 J, with a peak metabolic power of 83.5 W.

FEC and $\mathbf{W_{met}}$ The resultant scatter plot of morphology configurations that met the RMSE($\vec{M}$) $\leq$ RMSE($\vec{M}_{bio}$) criteria is plotted in Figure 2.9. Of the 500 morphology vectors sampled, 66 morphology vectors were recovered, with RMSE values ranging between 10.7 N-m and 6.21 N-m. Relative RMSE values are represented by both color and size; the range of colors from dark red to dark blue indicate a high RMSE and low RMSE respectively. Simillarly, the range from large markers to small markers indicate high and low RMSE values. A clear inverse relationship emerges among the filtered sets' FEC values and metabolic costs. A first-order polynomial fit yielded the regression estimate $W_{met_{Predict}} = -254.6J \times \text{FEC} + 135.1J$ with an R^2 value of .964.

Table 2.3: $\vec{M}_{bio}$ **and** $\vec{M}_{abs}$ **Morphology Comparison.**

Parameter	$\vec{M}_{bio}$	Normalized Value	$\vec{M}_{abs}$	Normalized Value	Δ (%)
$\mathbf{L_{MTU_0}}$ (m)	.366	$.915L_{shank}$	.363	$.908L_{shank}$	-0.8
$\mathbf{L_{CE_0}}$ (m)	.040	$.100L_{shank}$	.013	$.033L_{shank}$	-67.5
$\mathbf{L_{SEE_0}}$ (m)	.326	$.815L_{shank}$	.350	$.375L_{shank}$	+7.4
$\mathbf{K_t}$ (Nmm^{-1})	315.4	—	341.5	—	+8.3
$\mathbf{L_{CE}/L_{MTU}}$ (%)	10.8	—	3.67	—	-66.0
$\mathbf{F_{CE_{MAX}}}$ (N)	6000	—	6000	—	0.0
$\mathbf{V_{CE_{MAX}}}$ (ms^{-1})	.326	$8.24L_{CE_0}$	.110	$8.24L_{CE_0}$	-66.3
Peak $\alpha(\mathbf{t})$ (%)	95.3	—	83.4	—	-12.5
$\mathbf{W_{CE}^{+}}$ (J)	13.6	$.194\frac{J}{kg}$	3.71	$.053\frac{J}{kg}$	-72.7
FEC	0.349	—	0.481	—	+37.8
RMSE (N-m)	10.7	—	6.21	—	-42.0
$\mathbf{W_{met}}$ (J)	50.3	$.719\frac{J}{kg}$	14.2	$.203\frac{J}{kg}$	-71.8

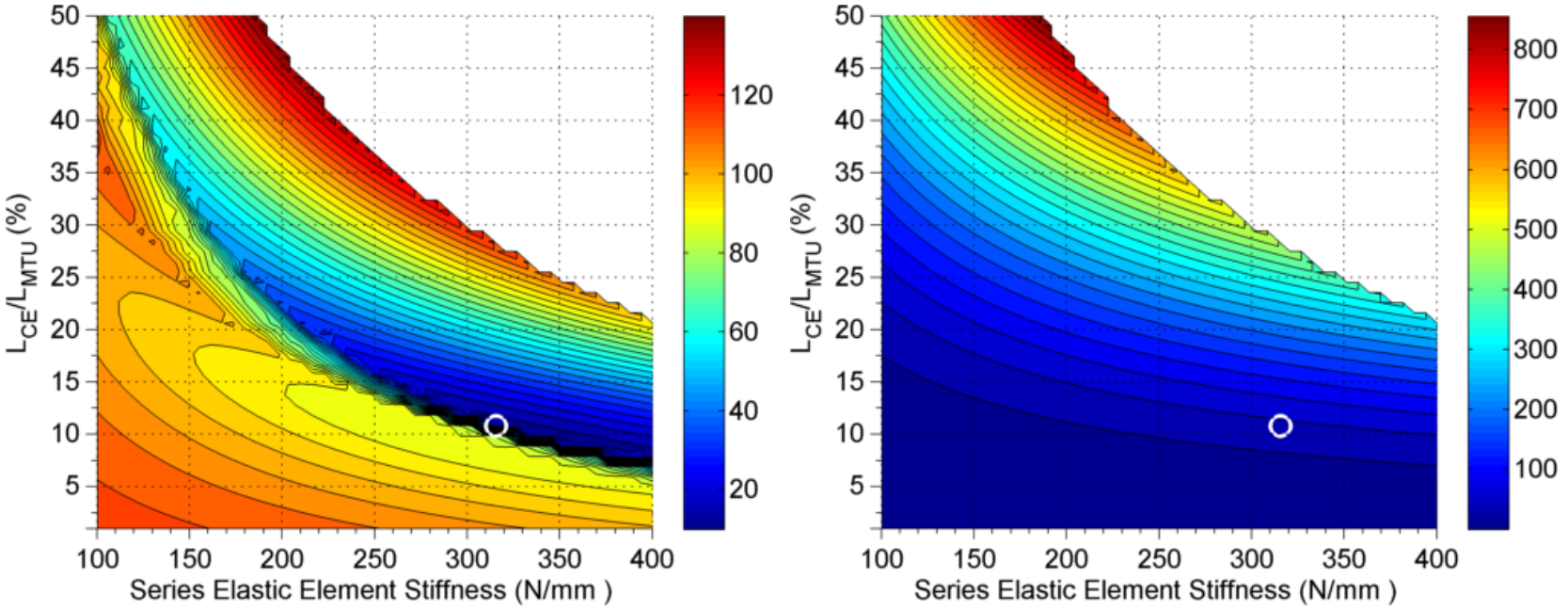

(a) (b)

Figure 2.5: **Contour maps of RMSE and metabolic cost for $^{L_{CE}}/_{L_{MTU}}$ percentages and K_t stiffnesses surrounding $\vec{M}_{bio}$ solution.** a) RMSE contour map of $\vec{M}_{bio}$. The minimum RMSE solution vector $\vec{M}_{bio}$ resolves at $\vec{M}_{bio}$ = [.366 m(L_{MTU_0}), .108 ($^{L_{CE}}/_{L_{MTU}}$), 315.4 $Nmm^{-1}(K_t)$] with an RMSD of 10.7 $N * m$ across the stride. b) The associated metabolic cost of $\vec{M}_{bio}$ is 50.3 J, with the minimum value for the contour existing along the $^{L_{CE}}/_{L_{MTU}} = 0$ plane. Both figures reside on the L_{MTU_0} = .366 m plane.

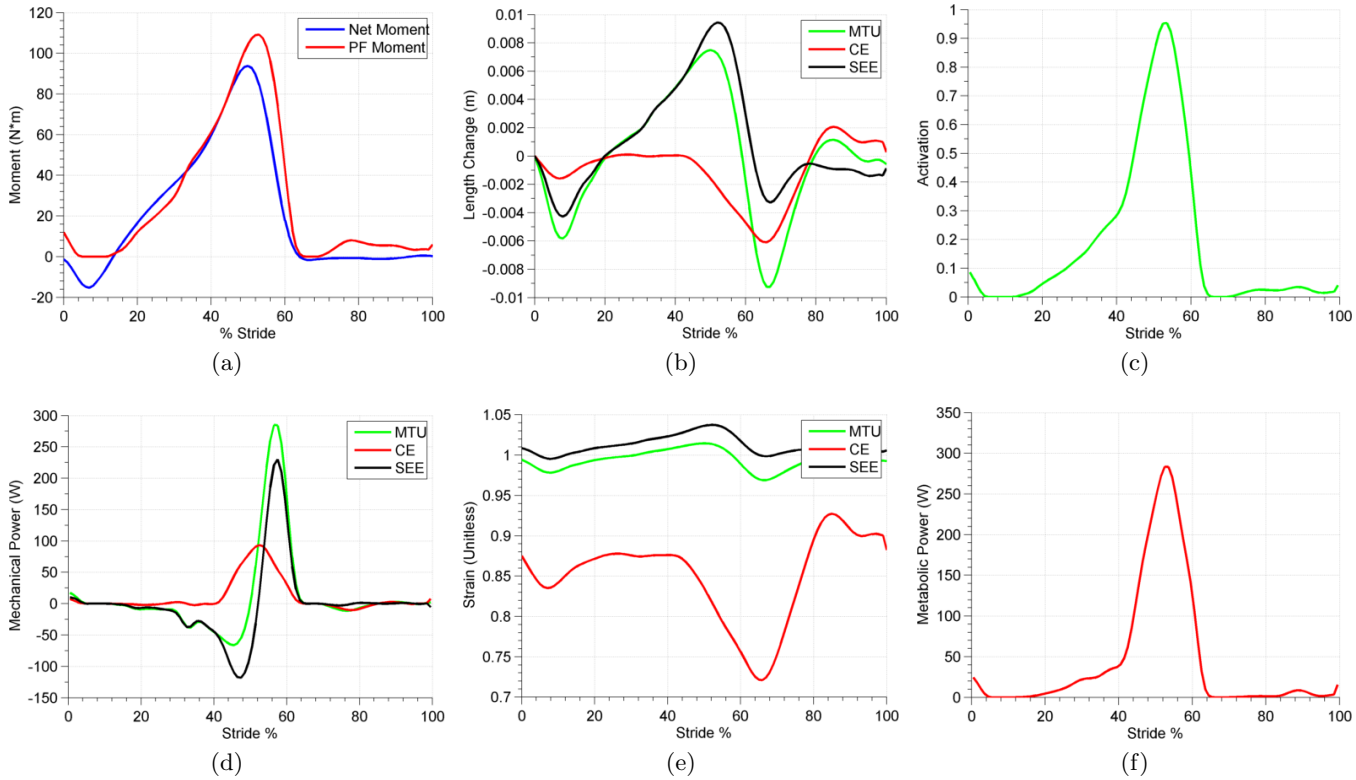

Figure 2.6: $\vec{M}_{bio}$ **solution MTU behavior.** a) $m_{model_{PF}}(\vec{M})$ and m_{net} profiles for solution vector $\vec{M}_{bio}$ = [.366 m, .108, 315.4 Nmm^{-1}] b.) Absolute length change of each MTU element. c) Requisite activation signal to maintain F_{CE} (t) and L_{CE} (t). d) Mechanical Power time series for MTU,CE,and SEE; Positive CE work across stride was 13.6 J. d) Strain profiles for MTU, CE, and SEE. f) Metabolic power during stride; total metabolic cost was 50.3 J.

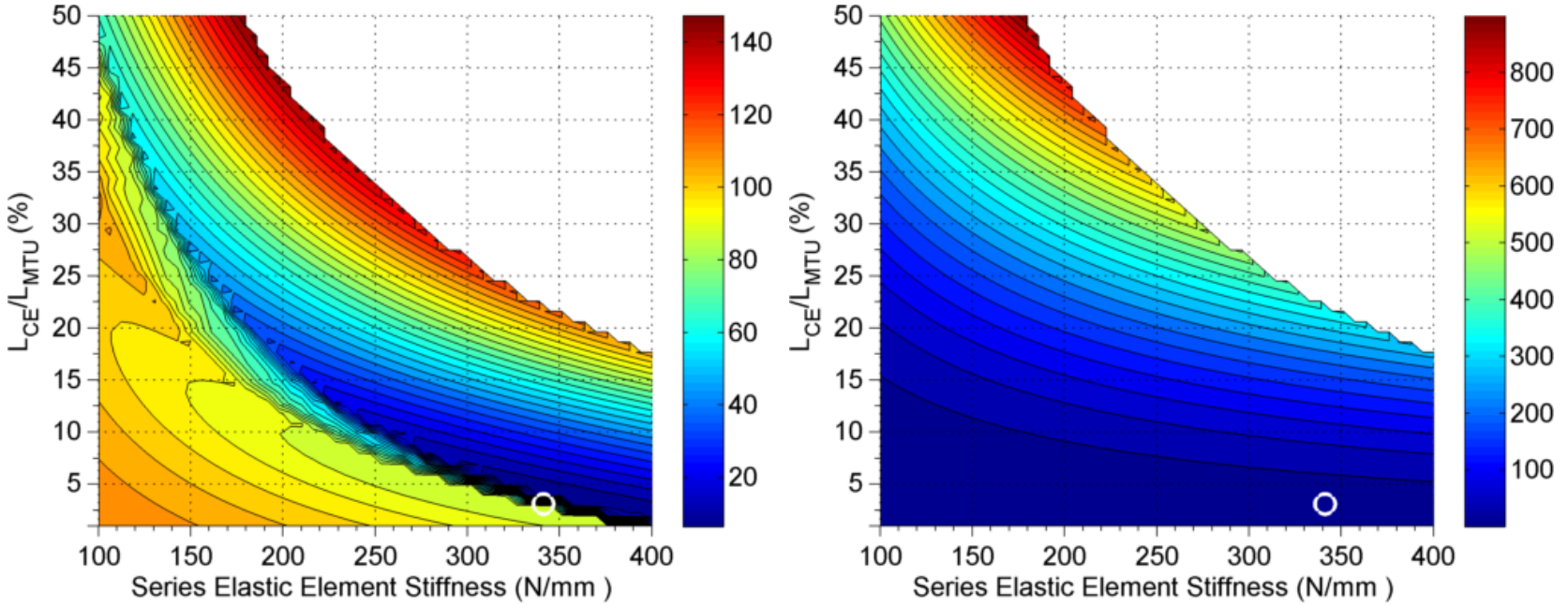

(a) (b)

Figure 2.7: **Contour maps of RMSE and metabolic cost for $^{L_{CE}}/_{L_{MTU}}$ percentages and K_t stiffneses surrounding $\vec{M}_{abs}$ solution.** a) RMSE contour map containing $\vec{M}_{abs}$. The minimum RMSE solution vector $\vec{M}_{abs}$ for all solution space resolves at $\vec{M}_{abs}$ =[.363 m (L_{MTU_0}), .0367 ($^{L_{CE}}/_{L_{MTU}}$), 341.5Nmm^{-1} (K_t)] with an RMSE of 6.21 N-m across the stride. b) The associated metabolic cost of $\vec{M}_{abs}$ was 14.2 J. The minimum metabolic cost solution vectors resolved along the $^{L_{CE}}/_{L_{MTU}} = 0$ plane. Both contour maps reside on the L_{MTU_0} =.363 m plane.

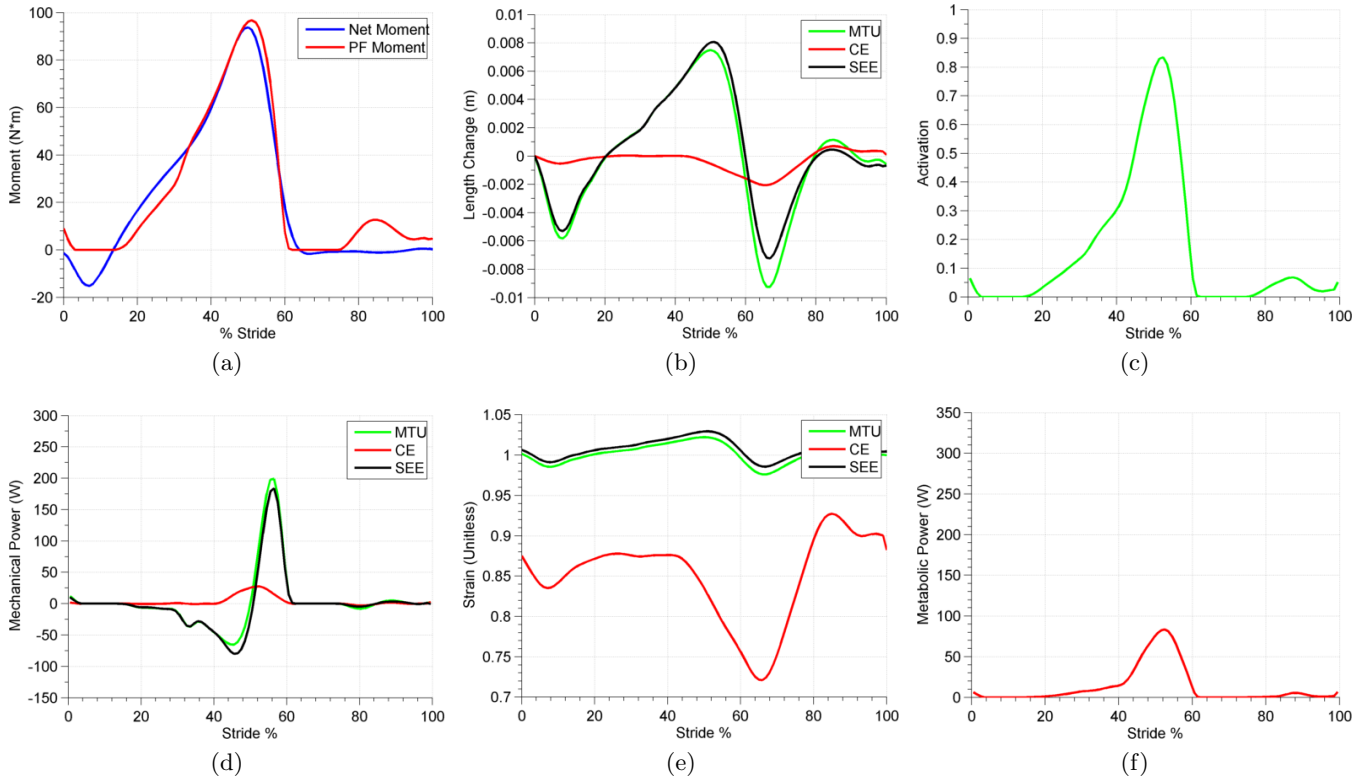

Figure 2.8: $\vec{M}_{abs}$ **solution MTU behavior.** a) $m_{model_{PF}}(\vec{M})$ and m_{net} profiles for solution vector $\vec{M}_{abs}$ =[.363 m (L_{MTU_0}), .0367 (L_{CE}/L_{MTU}), 341.5Nmm^{-1} (K_t)]. b) Absolute length change for each MTU element. c) Requisite activation signal to maintain F_{CE} (t) and L_{CE} (t). d) Mechanical power time series for MTU, CE, and SEE; Positive CE work across stridewas 3.71 J. e) Strain profiles of MTU, CE, and SEE. f) Metabolic power profile across stride; total metabolic cost was 14.2 J.

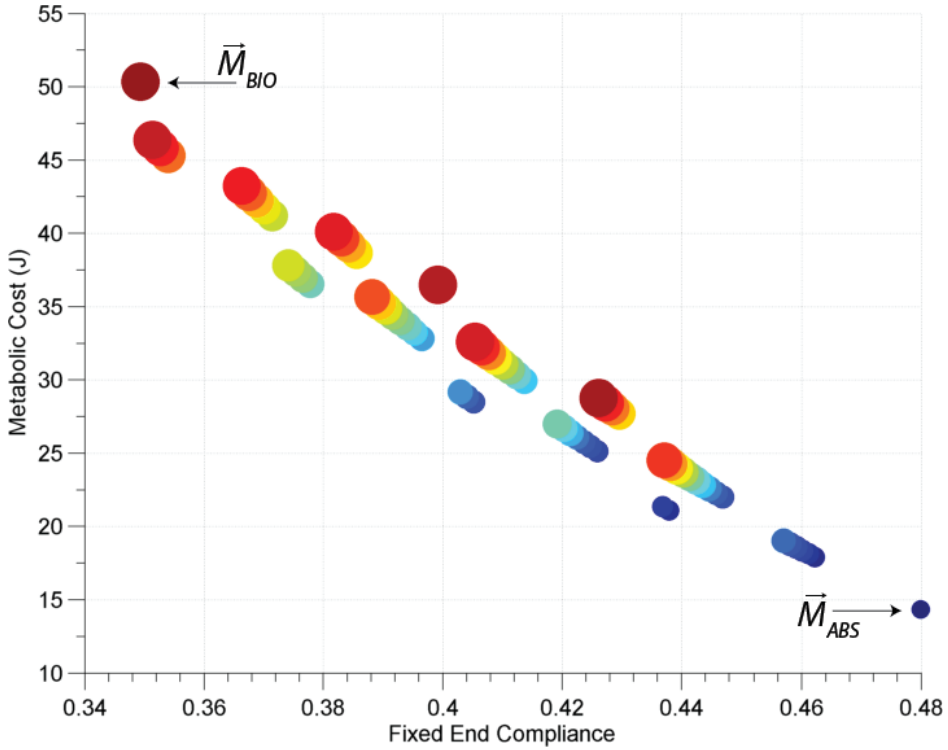

(a)

Figure 2.9: **Relationship between FEC and metabolic cost values of morphology configurations which produce "human-like" moments.** Figure displays a sample of 66 configurations found in parameter space between L_{MTU_0} = .366 m and L_{MTU_0} = .363 m which produced an RMSE value less than or equal to 10.7 N-m. Markers range in size and color to indicate range from high "human-like" RMSE values (dark red; large diameter) to low "human-like" RMSE values (dark blue, small diameter). The $\vec{M}_{bio}$ and $\vec{M}_{abs}$ solutions are the highest and lowest RMSE values, respectively, in this set.

2.4 Discussion

The goal of this study was to use a model driven by experimental data to examine the influence of muscle-tendon morphology on the mechanics and energetics of the ankle plantarflexors during human walking. The central question we sought to address was: what are the morphological features required to generate the lowest metabolic cost during walking at 1.25 ms^{-1}? Based on the premise that more compliant MTUs are best suited for metabolic economy[9], we hypothesized that, for solutions yielding human-like neuromechanics (i.e. muscle activation patterns and ankle joint moments), the metabolic energy expenditure would systematically decrease with increasing MTU compliance.

Our results strongly support the premise that compliance is inversly related to metabolic cost among plantarflexor morphologies that produce 'human-like' neuromechanics. Of the sampled morphology configurations that met the criteria RMSE($\vec{M}$) $\leq$ RMSE($\vec{M}_{bio}$), the corresponding FEC and metabolic cost values strongly fit a linear-regression estimate (R^2=.964) with a negative slope of -254.6 J and an intercept of 135.1 J(Figure 2.9).

More generally, our results suggest that more compliant muscle-tendon architectures are metabolically cheaper during human walking for any given error range. We found a distinct band of plantarflexor morphologies that produced 'low-error' ankle moments (RMSE $<$ 60 N-m) following a curved path in parameter space from [$^{L_{CE}}/_{L_{MTU}}$ = 50%, K_t = 100 Nmm^{-1}](FEC = 0.29) to [$^{L_{CE}}/_{L_{MTU}}$ = 7%, K_t = 400 Nmm^{-1}](FEC = .38) (Figure 2.5a). Along this path, the metabolic cost systematically decreased from 350.5 J to 41.0 J as the FEC increased from .29 to .38. If we relax the requirement that solutions produce low-error neuromechanics, it is possible to reduce the metabolic cost to zero for the most compliant case (W_{met} = 0 J at [$^{L_{CE}}/_{L_{MTU}}$ = 0%, K_t = 100 Nmm^{-1}]; FEC = ∞) (Figure 2.5b, bottom left corner). This is a somewhat trivial result because this plantarflexor morphology has no muscle(CE) and all tendon(SEE), and the stretch and recoil of the series elastic element (SEE) alone could not produce human-like ankle joint moments (RMSE = 116.1 N-m at [$^{L_{CE}}/_{L_{MTU}}$ = 0%,K_t = 100 Nmm^{-1}], FEC = ∞) (Figure 2.5a, bottom left corner). The result that plantarflexor morphologies that produced the lowest metabolic cost also produced the largest RMSE in the ankle joint moment and vice versa was consistent with findings of Krishnaswamy et al[43].

2.4.1 $\vec{M}_{bio}$ morphology, neuromechanics and energetics at preferred walking speed

The plantarflexor MTU architecture that generated the most human-like ($\vec{M}_{bio}$) neuromechanical output was consistent with experimentally reported values in the literature. This gave us confidence in the model despite its inherent simplicity (Table 2.3). Using a value for muscle

length ratio representative of the lumped plantarflexors (L_{CE}/L_{MTU} = 10.8%; see Methods for justification), $\vec{M}_{bio}$ required an L_{MTU_0} = 0.366 m and an SEE stiffness, K_t = 315.4Nmm^{-1} to most closely match the experimental net ankle moment (RMSE = 10.7 N-m; Table 2.3; Figure 2.5, open circles).

Muscle-tendon unit (MTU) geometry. In our model, the muscle-tendon unit (MTU) was intended to represent all three triceps surae MTUs, albeit in a reduced, uniarticular configuration (Figure 2.1). The total MTU slack length, L_{MTU_0}, comprises the sum of the L_{CE_0} and L_{SEE_0}. It is difficult to directly compare the L_{MTU_0} for $\vec{M}_{bio}$ with literature values because the origin and insertion of the lumped muscle in our model are not directly analogous to any one of the triceps surae MTUs (see Figure A.1a, b). However, our L_{MTU_0} of .366 m did fall within 1 SD of the SOL length reported by Ward ($.405 \pm 0.0832$ m)[64]. We note that Ward's value does not represent all connective tissue between the origin and insertion of the SOL, and is therefore not perfectly comparable to the $\vec{M}_{bio}$ L_{MTU_0}. Our value for L_{MTU_0} was also similar to those reported in recent modeling studies by Krishnaswamy et al. (SOL L_{MTU_0} = 0.255 m) and Arnold et al. (SOL L_{MTU_0} = 0.362 m)[7][43]. It is important to point out that most musculoskeletal models, including our own, assume the straight line attachment of an MTU between its origin and insertion. *In vivo*, MTUs have finite volume and often travel curved pathways. Given these constraints, it is not surprising that experimentally measured muscle lengths are often larger than values used in musculoskeletal models for a given MTU.

Contractile element (CE) geometry Our muscle contractile element (CE) length also compared favorably with soleus morphology values reported in the literature. The L_{CE_0} of $\vec{M}_{bio}$ was 0.040 m in length. This value is within 1 standard deviation (SD) of the experimentally captured L_{CE_0} (0.038 ± 0.007 m) that was reported for the normalized L_{CE} strain profile of the soleus (SOL) we used in our model ([58]). The L_{CE_0} also fell within 1 SD of the muscle architecture data for the SOL (0.044 ± 0.01 m), and within two standard deviations of the LG(0.059 ± 0.01 m) and MG(0.051 ± 0.01 m) reported by Ward ([64]).

Series elastic element (SEE) strain. Our $\vec{M}_{bio}$ morphology L_{SEE_0} (L_{SEE_0} = 0.326 m; Table 2.3) yielded series elastic element strains that are consistent with experimentally reported values for the triceps surae MTUs during walking. We note that experimental differences in strain between aponerouses, free tendons, and common tendons strongly suggest that connective tissues deform heterogeneously[4][50], a feature our model could not capture. In addition, our simplified model is meant to represent all connective tissues in the triceps surae, including the common tendon of MG, LG, and SOL MTUs, the free tendon of the MG and LG MTUs, and the respective distal and proximal aponeuroses of the MG, LG, and SOL. Despite the fact that

our model made gross simplifications to the anatomy of the connective tissues observed in vivo, it could still capture the overall strain behavior during walking quite well. In our model, the SEE strain for the $\vec{M}_{bio}$ solution peaked at 3.8% during the mid-stance phase ($\sim$ 50% of the stride) of walking (Figure 2.6e) . This value is consistent with reported strain values during walking for the medial gastrocnemius from both Lichtwark et al. ($\sim$ 3.8%)[48] and Arampatzis et al. (5.1% for the free tendon and 4.7% for the aponeurosis)[4], as well as strains reported for the soleus from Ishikawa et al.($\sim$ 6%)[39].

Series elastic element (SEE) stiffness (K_t). In our model, the $\vec{M}_{bio}$ SEE deformed to a peak excursion of $\sim$ 12.4 mm to produce a peak moment of 108.8 N-m (Figure 2.5b) and had a K_t = 315.4 Nmm^{-1} (equivalent to 530 $Nm * rad^{-1}$ (9.2 $Nm * deg^{-1}$)) (Table 2.3). Again, the heterogeneity of the strain profiles and material properties among different connective tissues make it difficult to directly compare our model series elastic stiffness (K_t) to experimentally measured stiffnesses. However, our value, meant to represent the combined stiffness of all elastic tissues in series with the triceps surae muscles, falls squarely within the range of experimental stiffness values reported for the tricep surae(180 Nmm^{-1} to 759 Nmm^{-1})(see Appendix A.4, Table A.1). Our value for K_t also compares well with the ankle plantarflexor SEE siffness values used in other computational modeling studies[6][43]. For example, Krishnaswamy et al. reported a combined average plantar flexor stiffness value of 375.6 N-m (+19.1%)[43].

Muscle-tendon unit (MTU) neural activation, mechanics and energetics The $\vec{M}_{bio}$ morphology parameters(Table 2.3) produced neural activation patterns, muscle-tendon interaction dynamics, and metabolic energetics consistent with experimental measures from walking at preferred speed(Figure 2.6). The neural activation pattern required to minimize the error between the model and experimental net ankle joint moment for $\vec{M}_{bio}$ had a timing and magnitude that mirrored both experimental and modeled activation profiles for the soleus muscle during walking at preferred speed[5][6][43][55][58][62]. Our peak muscle activation for $\vec{M}_{bio}$ in our model was 95.3% and occurred at $\sim$ 50% of the walking stride. This peak activation value was on the high end of reported values for soleus from other modeling studies (50%-80%) most likely because we enforced an experimentally measured soleus strain pattern(Figure 2.2 onto the lumped muscle that had rapid muscle shortening at the time of peak moment/force and requiring high activations to offset decreased force potential due to force-velocity effects.

Our modeled $\vec{M}_{bio}$ morphology and computed activation pattern generated muscle-tendon mechanics that agreed well with recent experimental reports for the whole ankle joint power output[24], as well as others that could partition mechanical power profiles of the MTU, CE and SEE components for medial gastrocnemius (MG) and soleus (SOL)[39] during walking. For example, the lumped MTU in our model generated mechanical power by storing a significant

amount of energy in the SEE through mid-stance and then releasing that elastic energy to provide $\sim$ 50% of the mechanical power output of the MTU during late stance (Figure 2.5d). These muscle-interaction dynamics are consistent with the catapult-mechanism reported by Ishikawa et al. for both MG and SOL[39], as well as the 50/50 power sharing reported by Farris et al. between the CE and SEE during the push-off power generation phase of walking at 1.25 ms^{-1}[24].

The time course of metabolic power(Figure 2.6f) consumed by the lumped plantarflexor model with the $\vec{M}_{bio}$ configuration was consistent with other model-based estimates for metabolic energy cost at preferred walking speeds. Umberger et al. estimated the metabolic power output for the plantarflexors using a forward dynamic simulation and reported a time course for metabolic power of the plantarflexors similar to ours, albeit with a much lower peak value ($\sim$100 W vs. $\sim$300 W) [62]. This discrepancy may arise from differences in the metabolic cost model and morphology parameters for the muscles and tendons between models. Krishnaswamy et al. also report peak metabolic power values for the combined plantarflexors that are lower than our estimate ($\sim$50W vs. $\sim$300W)[43]. A major difference in our models is that we imposed the experimental length change pattern for SOL[58], while Umberger et al. and Krishnaswamy et al. both estimated it using optimization, which may lend more credence to our result. On the other hand, our lumped model may fail to capture aspects critical to energetic cost estimates that are afforded by modeling all three triceps surae muscle independently.

Our model with $\vec{M}_{bio}$ consumed 50.3 J for a single plantar flexor, which gives us an estimate for the total cost of plantar flexor action per stride of 100.6 J for walking at 1.25 ms^{-1}. Sawicki et al.[60] used powered exoskeletons to estimate that the ankle MTUs consume $\sim$18% of the net metabolic energy over the limb ($\sim$308J) during walking at 1.25 ms^{-1}. Given that metabolic cost of standing is $\sim$1/3 of the net metabolic cost of preferred speed walking, we can assume that the gross metabolic cost is $\sim$400 J. This yields a rough estimate of 0.18×400 J = 72 J of metabolic energy for the plantarflexors - significantly lower than our model estimate. However, it is important to note that joint-level estimates of metabolic cost may underestimate *in vivo* energy expenditure of a muscle group, especially those with considerable series elastic tissues like the ankle plantarflexors. This is primarily due to lack of agreement between joint angular excursions and velocities and the length changes and velocities of the underlying muscles that determine metabolic cost.

2.4.2 Metabolically optimal plantarflexor morphology($\vec{M}_{abs}$) at preferred walking speed

Interestingly, the most human-like morphology $\vec{M}_{bio}$ did not result in the lowest metabolic cost solution. In fact, a metabolically cheaper solution, $\vec{M}_{abs}$, existed nearby in parameter space

at an L_{MTU_0} of .363 m (-0.8%), with a L_{CE_0} of .013 m (-67.5%) and a linear stiffness K_t of 341.5 Nmm^{-1} (+8.3%) (Table 2.3, Figure 2.7, white circles). In line with our central hypothesis, increasing the compliance of the MTU(FEC($\vec{M}_{abs}$) = 0.48 vs. FEC($\vec{M}_{bio}$) = 0.35) resulted in a lower metabolic cost solution (-71.8% compared to $\vec{M}_{bio}$). Using a shorter CE coupled with a stiffer SEE, $\vec{M}_{abs}$ could generate adequate moments with lower metabolic cost by virtue of a smaller activation coupled with a smaller $V_{CE_{MAX}}$. The F-V coefficients for the $\vec{M}_{abs}$ CE are lower than $\vec{M}_{bio}$ despite having the same L_{CE} profile and a proportional $V_{CE_{MAX}}$ (due to $V_{CE_{MAX}}$ relationship of the F-V curves (Eq. 2.5, Eq. 2.6), and consequently operate in a less advantageous space on the force-velocity curve for producing muscle activation. However, because the closer moment match of the $\vec{M}_{abs}$ solution(Figure 2.8a), the direct effect of lower relative forces of the $\vec{M}_{abs}$ solution dominate the inverse effect of having lower F-V coefficients for an overall decrease in CE activation (-12.5% compared to $\vec{M}_{bio}$)(Eq. 2.1). As activation is directly proportional to metabolic power(Eq. 2.14), a lower activation lowers the metabolic cost. Though the velocity coefficients in the metabolic function $f_{met}(\widetilde{V_{CE}})$ increase metabolic cost, the combined effect of the activation and lower $V_{CE_{MAX}}$ lower the W_{met} from 50.3 J to 14.2 J(Eq. 2.14).

Lower absolute velocities in the CE also resulted in reduced peak power outputs in $\vec{M}_{abs}$ vs. $\vec{M}_{bio}$ that limited its ability to contribute to total MTU power output from the recoiling SEE near the end of the stance phase (Figure 2.8d). Thus, although $\vec{M}_{abs}$ reduced metabolic cost compared with $\vec{M}_{bio}$, it had a negative impact on overall mechanical power output of the MTU. This hints at a potentially important trade-off between metabolic economy and high peak power outputs for the ankle plantarflexors. Though our lumped uniarticular model is too simple to address it, other modeling studies with more detailed anatomy have suggested that the redundancy afforded by having both biarticular (i.e. LG and MG) and uniarticular (i.e. SOL) MTUs across the ankle may be able to achieve high power output and metabolic economy simultaneously[43]. Along these lines, it may be that human plantarflexor morphology is uniquely tuned to maximize both metabolic economy and mechnical power output.

2.4.3 Potential limitations of a lumped, uniarticular plantarflexor muscle-tendon model

The conclusions of this study are predicated on the model retaining enough complexity to adequately capture all relevant features and behaviors in the major ankle plantarflexors (i.e. the triceps surae). Our choice to use a lumped uniarticular configuration to represent the triceps surae resulted in $\vec{M}_{bio}$ and $\vec{M}_{abs}$ solutions, and largely recovered the neuromechanics and energetic features observed in plantar flexors during human walking. However, it is important to address key generalizations implemented in this model that may have influenced the results

and their interpretation.

We chose to constrain MTU attachment sites to emulate a uniarticular MTU - therefore, MTU excursions were most consistent with the uniarticular soleus (see Appendix A.1. for more details). We made this choice because the soleus makes up the largest portion of the triceps surae total cross sectional area ($\sim$ 63%)[64]. However, the exclusion of biarticular MTUs prohibits the influence of the knee angle on the ankle joint moment. Thus, by neglecting to include biarticular MTU attachments, this study reduced the modulation of the triceps surae L_{MTU} to a function of the ankle joint angle only. For example, the gastrocnemius MTU length changes due to changes in knee joint angle are nontrivial during walking, and when considering the order of magnitude of series elastic tissue stiffnesses, even extra millimeters of deflection could generate significant changes in net ankle joint moments. Failing to represent the influence of knee angle on plantar flexor moment generation likely contributed to the mismatch in the net ankle moment produced by both $\vec{M}_{bio}$ and $\vec{M}_{abs}$ solutions when compared to experimental data (Figure 2.6a, Figure 2.8a). We further note that, in general, the severe gradients surrounding minimum regions of the RMSE contours (Figure 2.5a, Figure 2.7a, Appendix A.3) suggest that for the attachment and insertions sites we implemented in our model, the net ankle joint moment is highly sensitivity to variations in overall MTU length. For example, a relatively small 0.003 m reduction in L_{MTU_0} of the $\vec{M}_{bio}$ vector (i.e. the L_{MTU_0} plane where $\vec{M}_{abs}$ resided) resulted in a RMSE value change from 10.7 N-m to 32.7 N-m.

Consolidating all three triceps surae muscles (MG, LG and SOL) into a single uniarticular muscle reduces the neuromotor degrees of freedom exhibited by the human plantar flexor system *in vivo*. Each of the tricep surae muscles in a human leg is modulated according to its own neural control signal. These unique activation patterns separately influence the respective CE length changes, forces, and metabolic energy consumption for the SOL, LG, and MG. This affords redundancy that likely expands the suite of behaviors beyond what our lumped model can capture. However, in spite of using a common motor drive, our model accurately recovered both the timing and magnitude of activation exhibited by the plantarflexors on average during preferred speed walking (Figure 2.6c, Figure 2.8c).

By enforcing an experimental SOL strain pattern, we implicitly assumed that it adequately represented the strain patterns in the other triceps surae muscle. Again, we chose to base our model on SOL since it has the largest physiological cross sectional area within the triceps surae group and likely contributes the majority of plantarflexor moment[43][64]. However, imaging studies performed on the LG and MG have demonstrated that the gastrocnemius exhibits a distinct, albeit similar, excursion pattern when compared to SOL[39]. Small differences in the timing of muscle shortening could have a large impact on the activation required and, by extension, the metabolic energy cost to generate the peak plantarflexor moments with timing observed during human walking. For example, the rapid shortening just prior to toe off exhibited

by the L_{CE} in our model requires a much larger activation signal than a CE length change pattern that would undergo shortening later with respect to the time of peak ankle moment. Both experiments and models indicate that the gastrocnemius reaches its maximum shortening velocity after the soleus and the time of peak plantarflexor moment[22][43]. Thus, leaving out the gastrocnemius in our model may have biased absolute values of muscle activation and metabolic power upward. Despite this limitation, the conclusion that higher increased MTU compliance results in lower metabolic cost should still hold.

Though we aimed to conserve experimentally established muscle-tendon properties and constitutive relationships governing muscle force production for the human plantar flexors[58][64] in our model, there were a number of mechanisms that we did not include. For example, it is well known that pennation angle changes dynamically during the course of a contraction[8]. This variable gearing behavior plays a crucial role in pennate muscles like the triceps surae because it can change the component of fascicle force that acts in line with the series elastic tissues on the input moment arm of the ankle joint. However, the variable gearing effect is force dependent, and therefore has a small effect late in stance when activations and metabolic expenditure are highest during human walking. For this reason, we felt the added complexity would not influence our main conclusion that compliance is directly related to metabolic economy of the plantarflexors.

Finally, we did not take into account the possibility that a muscle maximum force might scale with its length. $F_{CE_{MAX}}$ was set at 6000 N, which was chosen to be within the range of maximum force values for the combined triceps surae muscle group used by other models in the literature[7][43]. We used this value for all morphologies, based on the idea that each of our morphologies would have the same physiological cross sectional area (i.e. no imposed volume constraint). Another approach would be to scale $F_{CE_{MAX}}$ with L_{CE} so that longer CEs would also have higher $F_{CE_{MAX}}$ values.

2.4.4 Future Directions

The simple modeling framework and associated data-driven computational approach that we have developed and presented in this study could be extended to address a number of additional questions moving forward. We focused our efforts in this study on examining the metabolic cost of many different plantarflexor MTU morphologies defined by combinations of L_{MTU_0}, $^{L_{CE}}/_{L_{MTU}}$, and K_t, during human walking at preferred speed. With experimental data for joint angles, joint moments and fascicle strain patterns, the same inverse approach could be applied to walking or running at different speeds, or on different surface gradients or with carried loads. It would also be possible to extend the methodology to examine the morphology space of muscle-tendons crossing the knee or hip where different morphological features (e.g.

PCSA) and/or assessment metrics (e.g. maximal MTU power generation or maximal MTU power absorption) might be more important.

From a more clinical and applied science standpoint, we recognize the possibility that the experimental inputs and model parameters could be appropriately adapted to address the question of how altered MTU morphology following neurological (e.g stroke, spinal cord injury, cerebral palsy) or musculoskeletal (i.e. Achilles tendon rupture) injury might influence the form-function relationships for different MTUs of the lower-limb.

Finally, the model results for $\vec{M}_{bio}$ that we presented in this study effectively capture the most crucial behaviors observed in the human triceps surae during human walking (e.g. the catapult mechanism). This gives us confidence in using the human-like $\vec{M}_{bio}$ solution as the basis for an *in silico* framework that can be applied to optimize the parameters of assitive devices designed to be worn in parallel with the human ankle plantarflexors (i.e. passive or active exoskeletons[66]). Future studies should aim to incorporate simple mechanical models for actuators and/or passive elastic elements acting in parallel with the current model. Then, assuming that humans maintain the same overall joint mechanics[41], it should be possible to predict and ultimately optimize the interaction between wearable devices and to achieve desired behaviors of the underlying biological system.

Chapter 3

Modeling the Influence of Elastic Ankle Exoskeleton Stiffness on Plantar Flexor Muscle-tendon Interaction during Human Walking

3.1 Introduction

Human walking[30], hopping[20], and running[10][53] all exhibit compliant dynamics that can be captured by simple spring-mass models. In essense, the lower-limb is able to compress and recoil elastically with stiffness that arises from the combination of passive, non-linear material properties of the muscles and series elastic connective tissues, and active neuromuscular control and reflex feedback. During locomotion, "springy-limbs" enable a number of elastic mechanism that are exploited to improve performance. For example, properly timed stretch and recoil of series elastic tissues can be used to enhance muscle power output during acceleration, attenuate muscle power requirements during deceleration, or conserve mechanical and metabolic energy during steady speed locomotion[57].

The range of performance benefits afforded by compliant limbs in humans and animals has inspired wearable exoskeletons that may have applications in both gait rehabilitation and augmentation. Recently, a number of lower-limb exoskeletons have been developed that use elastic elements (i.e. springs and clutches) in parallel with the limb to strategically store and return energy and help power locomotion[25][33][66]. Physiological measurements in studies of vertical hopping in elastic exoskeletons spanning the whole limb[33], the knee joint[15][19][23], and the ankle joint[25] indicated performance benefits that include reduced muscle activity, reduced

biological limb/joint stiffness and mechanical power output, and reduced metabolic energy cost of the user. These studies of simple movements like vertical hopping have paved the way for the development and implementation of elastic exoskeletons to improve user performance during human walking and running gaits.

During human walking, the majority of mechanical power comes from the ankle plantarflexors [24]. Furthermore, approximately half of the requisite mechanical power output at the ankle comes from elastic recoil of the Achilles tendon at "push-off"[22]. Given the plantarflexors primary role in forward propulsion[32] and the significant elastic mechanism afforded by their compliant muscle-tendon architecture, the ankle joint seems to be a logical site for a passive elastic exoskeleton that can improve human walking performance.

There are a number of unique challenges in developing a passive elastic exoskeleton that can assist the ankle plantarflexors during walking. In more prototypical bouncing gaits like vertical hopping and running, highly symmetrical loading /unloading cycles enable easy integration of a parallel spring. In these devices, a spring rest length is merely set to correspond with the prescribed leg length or joint angle at the onset of the ground contact phase. Furthermore, the spring does not need to be explicitly disengaged because the leg/joint posture alone can modulate spring slack and tension with the appropriate pattern[14][25][33]. In constrast, during walking, the triceps surae muscle-tendons (soleus, medial and lateral gastrocnemius) all undergo an asymmetric length change pattern with slow lengthening over the majority of stance ($\sim$10%-50% of the stride), followed by rapid shortening. This length change pattern is indicative of a catapult mechanism whereby elastic energy slowly builds up in the Achilles tendon as it is held by a highly active, nearly isometric muscle. Stored elastic energy is then rapidly released in a burst of mechanical power at push-off[39]. Finally, the slackened plantarflexors re-lengthen during swing phase to reset for the next heel-strike. Thus, in order to emulate the catapult mechanism observed during walking, a passive elastic ankle exoskeleton with a parallel spring acting as an exo-tendon would have to deliver energy to the ankle during the push-off phase of walking while allowing the ankle to freely rotate during swing phase. Due to the aforementioned asymmetry in the ankle joint angle during walking, the anchored spring design used in previously developed hopping ankle orthoses[23][25] cannot store appropriate amounts of elastic energy during stance phase without imposing a significant metabolic penalty to re-stretch the spring and reset the foot during swing.

We have developed a novel, passive elastic ankle-foot orthosis (AFO) that can store and return energy during the stance phase while allowing free ankle rotation during the swing phase of walking[66]. The key feature in the design is a rotary clutch that uses a ratchet and pawl configuration and two timing pins set to engage and disengage the exoskeleton spring at set ankle joint angles(Figure 3.1a). The exoskeleton spring is engaged when the first timing pin pushes the pawl onto the ratchet at terminal swing, where the ankle dorsiflexes just prior

to heel strike. This enables the spring to store and return elastic energy during stance. Then, once the ankle reaches extreme plantarflexion, after the foot is off the ground, a second timing pin pushes the pawl off of the ratchet, allowing the user to freely rotate their foot without interference from the exoskeleton spring. This AFO design is simple, lightweight($\sim$ 300 g), and requires no electronics or battery, making it a low cost option for gait assistance. The immediate goal of this device is to reduce the metabolic cost of human walking, but it is not clear what the stiffness of the parallel spring (i.e. "exo-tendon") should be in order to minimize the energy consumption of the user[13].

The goal of this study was to develop a simple, data-driven computational model of a passive elastic ankle exoskeleton[66] working in parallel to the human ankle plantarflexors. We employed a model to understand how compliant mechanical assistance impacts underlying muscle-tendon mechanics and energetics during level walking at preferred speed. More specifically, we aimed to address two questions: (1) what is the relationship between elastic ankle exoskeleton spring stiffness and the metabolic cost incurred by the users plantarflexors during walking at 1.25 ms^{-1}?; and (2) how does a spring in parallel with the ankle plantarflexors impact the mechanics of the underlying "catapult mechanism"? Humans tend to reduce their biological ankle moment contribution in order to maintain consistent overall ankle joint kinetics during locomotion with ankle orthoses[12][14][21][23][25][41]. In line with this adaptive behavior, we hypothesized that higher exoskeleton stiffness would result in larger reductions in the metabolic cost of the

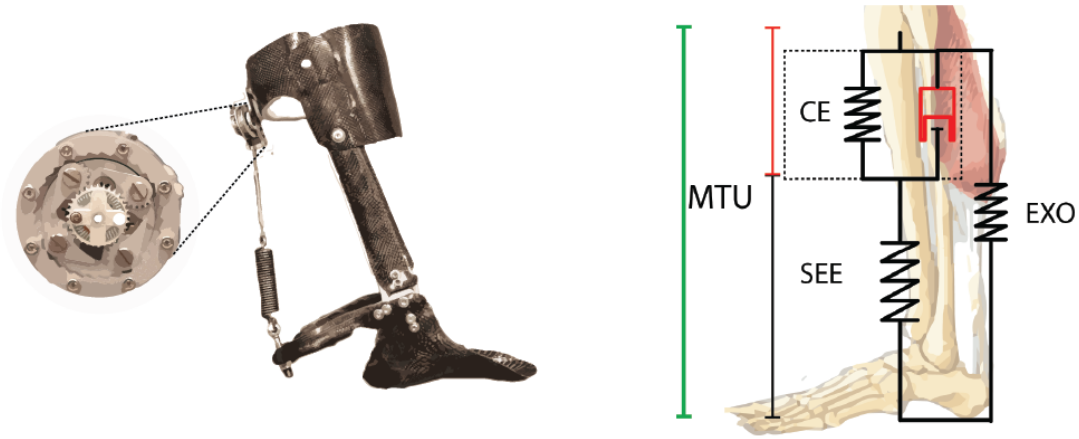

(a) (b)

Figure 3.1: **Passive EXO developed by Wiggen et al.[66] and component representation in lumped model.** a) Rotary clutch with ratchet and pawl mechanism developed by Wiggen et al.(*left*), and the exoskeleton that houses it(*right*). b) The clutched-spring was represented as spring component EXO. L_{EXO} was identical to L_{MTU} for all points in the stride.

plantarflexors during walking. In addition, we expected that elastic ankle exoskeletons would disrupt the normal "catapult mechanism" exhibited by the ankle plantarflexors. That is, as parallel spring stiffness increases and the exoskeleton takes over more and more of the plantarflexor moment, the Achilles' tendon should undergo less stretch requiring larger excursions of the muscles fascicles in series. Higher muscle shortening velocities are more metabolically costly. Thus, despite lower force/moment requirements, it is possible that higher shortening velocities could increase metabolic energy requirements in the plantarflexor muscles and offset the potential benefit of increased assistance from elastic ankle exoskeletons.

To address the hypotheses, we extended our previous model of the ankle plantarflexors in Khan et al., Chapter 2[42] to include a spring in parallel with the biological muscle-tendon unit (i.e. an elastic ankle exoskeleton). Then, using the morphology parameters and neural activation timing that generated human-like ($\vec{M}_{bio}$) ankle neuromechanics and energetics, we simulated many combinations of muscle activation amplitude and parallel spring stiffness to predict the total (biological + exoskeleton) ankle joint moment, the metabolic energy consumption, and muscle-tendon interaction dynamics of the biological muscle-tendon unit. Finally, we note that the benefit of employing simple models such as this one to aid the design and optimization of assistive devices cannot be overstated, as the time and effort to build custom devices for many individuals and conduct well controlled human performance studies is extensive[13].

3.2 Methods

3.2.1 Model Composition

Base MTU model. The base muscle model utilized in this study was parameterized identically to the $\vec{M}_{bio}$ configuration of the model used in Khan et al., Chapter 2[42]. A uniarticular Hill-Type muscle-tendon unit(MTU), representative of the all contractile tissue and connective tissue between the origin and insertion of the triceps surae muscle group, was simulated with a contractile element(CE), representing the contracting functionality of the muscle bodies, and a series elastic element(SEE), representing all other connective tissues including tendons, tendinous attachments, and aponeuroses[67]. The CE was parameterized with an optimal operating length L_{CE_0}, of .04 m, an $F_{CE_{MAX}}$ of 6000 N, and a $V_{CE_{MAX}}$ of $8.24\times L_{CE_0}$ ms^{-1}. The SEE was parameterized with a slack length L_{SEE_0}, of .326 m, and a linear stiffness K_t of 315.4 Nmm^{-1}. The sum of L_{CE_0} and L_{SEE_0} is the resultant MTU slack length, L_{MTU_0}. The force dynamics of the CE and SEE were also modeled in accordance with the force charactertics described in Khan et al., Section 2.2[42].

Elastic exoskeleton element. The lumped muscle model configured to $\vec{M}_{bio}$ was modified to include an additional passive element, EXO, operating in parallel with the MTU(Figure 3.1b). EXO was based on the clutched-spring passive AFO developed by Wiggin et al.[66], which utilizes a clutch to strategically engage and release a spring according to ankle angle. The details of clutch function is described in [66].

The effective slack length of the EXO spring, L_{EXO_0}, was the MTU length at which the ankle angle transitioned into dorsiflexion after heel strike(Eq. 3.2). After this point, the EXO spring stored and released energy until the second transition from plantar flexion to dorsiflexion, at which time EXO force generation capability was terminated (i.e, shortly before swing)(Figure 3.2). EXO force generation was modeled with a hookean force-length relationship where a stiffness K_{EXO} dictated the force-length slope (Eq. 3.3, Eq. 3.4).

$$L_{EXO} = L_{MTU} \tag{3.1}$$

$$L_{EXO_0} = L_{MTU}(t) \text{ where } \frac{d\Theta_{Ankle}}{dt} = 0 \text{ and } \frac{d^2\Theta_{Ankle}}{dt^2} > 0 \text{ shortly after heel strike.} \tag{3.2}$$

$$F_{EXO} = K_{EXO} \times (L_{EXO} - L_{EXO_0}), \quad L_{EXO} > L_{EXO_0} \tag{3.3}$$

$$F_{EXO} = 0, \quad L_{EXO} < L_{EXO_0} \tag{3.4}$$

The EXO was modeled with the same moment arm as the MTU throughout the stride.

3.2.2 Forward Framework

The feed forward model took a vector $\vec{M}_{EXO}$ composed of an EXO stiffness K_{EXO} and and activation scaling constant c. The CE, configured to the $\vec{M}_{bio}$ solution length, was then activated according to the activation profile $\alpha(t)$ produced by the $\vec{M}_{bio}$ but scaled to scaling constant c. The EXO element generated a force according to stiffness K_{EXO}, and the resulting moments created by both the MTU and EXO combined to m_{ankle}.

The L_{MTU} for all ankle angles in the stride were calcuated. For all lengths of the MTU,

$$L_{MTU}(t) = L_{CE}(t) + L_{SEE}(t). \tag{3.5}$$

Because the CE and the SEE are in series,

$$F_{MTU} = F_{CE} = F_{SEE}. \tag{3.6}$$

The CE was activated with with $c * \alpha(t)$ for each point in the stride, and the L_{CE} and L_{SEE} lengths were calculated such that the equilibrium $F_{SEE} = F_{CE}$ was achieved. F_{EXO} was simultaneously calculated for the stride using Eq. 3.3 and Eq. 3.4. F_{ANKLE} was calculated in

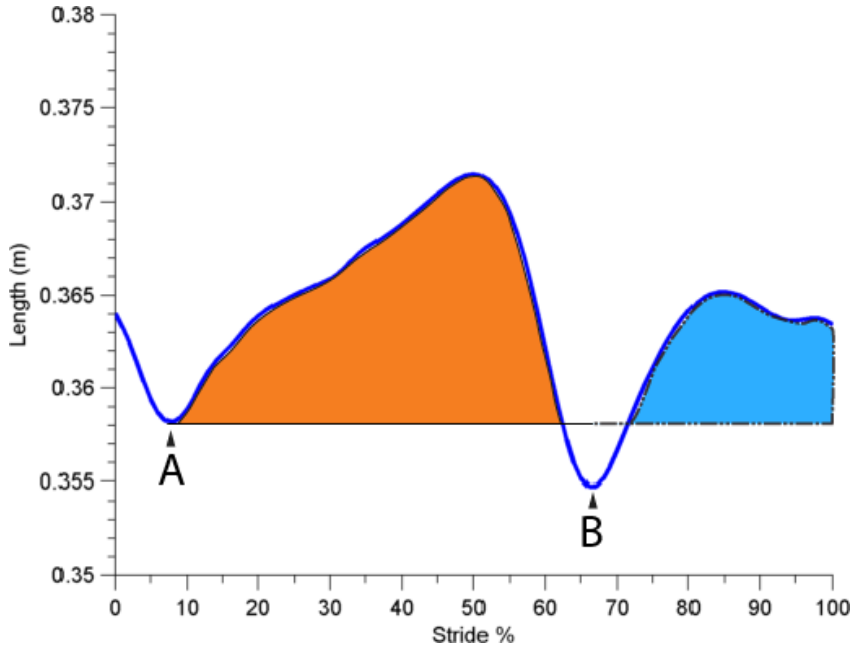

(a)

Figure 3.2: **EXO engagement across L_{MTU} values in stride.** Point **A** represents the MTU/EXO length at which the EXO spring would stretch(Eq. 3.2). EXO energy storage and release would occur until L_{MTU} fell below L_{EXO_0} (*area shaded orange*). The simulated EXO disengaged at point **B**, enabling joint posturing for swing phase without changing the length of the EXO spring and storing energy during the swing (*area shaded in blue*).

accordance with the equation

$$F_{EXO} + F_{MTU} = F_{ANKLE}.$$

Since the MTU and EXO act in parallel along identical moment arms, F_{ANKLE} was then multiplied by effective moment arm throughout the stride to determine the m_{ankle} profile. The RMSE between the m_{ankle} and the plantar flexor profile generated using the $\vec{M}_{bio}$ solution, m_{PF}, was then calculated. Lastly, the metabolic cost for the $\vec{M}_{EXO}$ solution was computed(Eq. 2.17).

Forward implementation. Using the framework defined above, K_{EXO} and c were systematically varied to generate an RMSE and metabolic cost contour map for each vector(Figure 3.3).

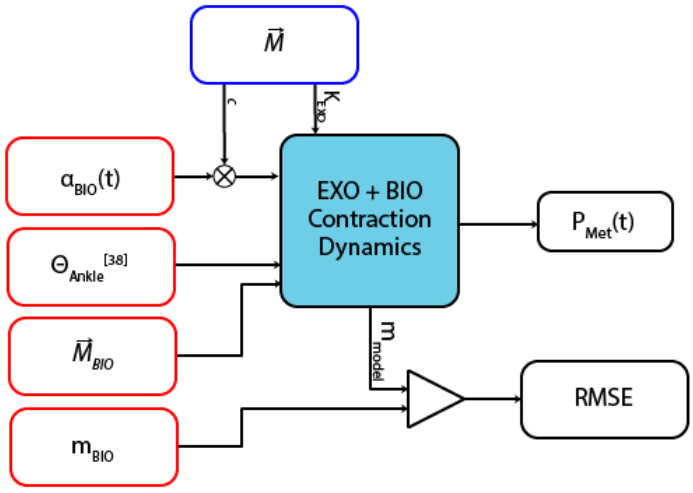

Figure 3.3: **Simplified block diagram of forward framework inputs and outputs.** Variable input $\tilde{\mathbf{M}}$ is outlined in blue, experimental profiles are outlined in red, and outputs are outlined in black.

3.2.3 Inverse Framework

The inverse approach implementation sought to conserve the plantar flexor profile m_{PF}, generated by the $\vec{M}_{bio}$ solution. The m_{PF} was divided by the moment arm throughout the stride to determine the necessary plantar flexion force profile F_{PF}.

A spring stiffness K_{EXO} was defined, and F_{EXO} was calculated for each point in the stride according to Eq. 3.3. Since m_{PF}, and by extension F_{PF}, had to be conserved, F_{EXO} was

subtracted from F_{PF} to calculate the requisite F_{MTU} profile. However, in order to perfectly conserve F_{PF}, F_{EXO} was forced to F_{PF} if Eq. 3.3 would have exceeded F_{PF} at any point in the stride. Any F_{EXO} produced that does exceed F_{PF} would have to be compensated for by the antagonist muscle compartment (i.e. tibialis anterior) to conserve the m_{net} profile.

The L_{SEE} values that mapped to the F_{MTU} were calculated. Each L_{SEE} length was then subtracted from the L_{MTU} profile to determine the L_{CE} profile needed to maintain the MTU lengths. With L_{CE} defined for all points during the stride, V_{CE} was calculated by taking the difference between every point. Eq. 2.1 was then used to calculate the activation signal α profile necessary to produce F_{MTU}. Finally, the mechanical power, average positive mechanical work, metabolic power, and total metabolic work were then calculated in accordance with Eq. 2.12, Eq. 2.13, and Eq. 2.17 to assess performance.

Compensatory metabolic cost A compensatory metabolic cost was also calculated for K_{EXO} values in which F_{EXO} would exceed F_{PF} and generate an excess moment per Eq. 3.3(prior to being artificially limited to F_{PF} for inverse calculation reasons). These moments would have to be generated by the dorsiflexor antagonist group to preserve m_{net} (Figure 2.2a. The compensatory metabolic cost was estimated using the average metabolic cost of a N-m during a stride with the $\vec{M}_{bio}$ solution. The excess F_{EXO} force was multiplied by the moment arm and was scaled to the average metabolic cost per N-m to determine the compensatory metabolic cost.

Inverse implementation. The inverse simulation framework was computed for K_{EXO} values between 0% and 100% of 315.4 Nmm^{-1}. Behaviors of the CE, SEE, and EXO were than quantitatively characterized.Figure 3.4 displays a simplified block diagram of the inverse framework.

3.3 Results

3.3.1 Forward Results

The contour maps of the forward simulation results are displayed in Figure 3.5. The minimum RMSE in Figure 3.5a resides at $\vec{M}_{EXO}$ = [0 Nmm^{-1} (K_{EXO}), 1 (scaling constant c)]. This is the singular minimum on the parameter plane; no other $\vec{M}_{EXO}$ solution achieves the [0,0] RMSE. All other solutions increasingly aggregate moment error along either axis. However, a linear depression exists on the contour between [0,1] to [.60, 0]. Figure 3.5b shows the metabolic expenditure for the same parameter plane. Metabolic cost of the model was only related to activation scaling constant c, which was trivially minimized at the $c * \alpha(t)$ plane of 0.

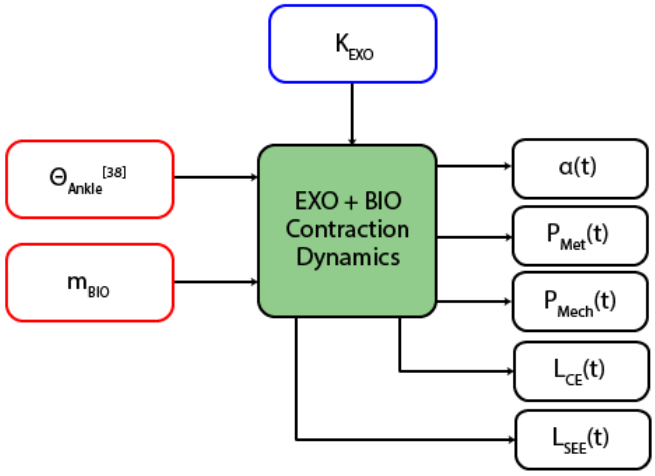

Figure 3.4: **Simplified block diagram of inverse framework inputs and outputs.** Variable input $\tilde{\mathbf{M}}$ is outlined in blue, experimental profiles are outlined in red, and outputs are outlined in black.

3.3.2 Inverse Results

Figure 3.6 displays normalized representations of element forces, activations, metabolic costs, and mechanical work for the range of K_{EXO} values from 0% to 97% $\vec{M}_{bio}$ K_t. After K_{EXO} = 97%, the CE velocity surpassed the $V_{CE_{MAX}}$ capacity set and was unable to recover an MTU activation profile that would recover the $\vec{M}_{bio}$ moment profile. Total ankle force F_{ANKLE}, F_{EXO}, the active contribution of F_{CE}, and the passive contribution of F_{CE} were summed together and normalized to the summed F_{PF} across the stride in Figure 3.6a. F_{ANKLE} remains at a normalized value of 1 until $K_{EXO} = 44\%$, where the total F_{ANKLE} force begins to increase. The normalized ideal F_{EXO} (i.e. F_{EXO} that does not surpass necessary F_{PF} profile) contribution increases almost linearly until it saturates all of the F_{PF} profile that it is engaged for. Contrasingly, the F_{MTU} decreases until it provides the F_{PF} portions where the EXO is not engaged. Finally, the passive contribution of F_{CE} is 0 until $K_{EXO} = 44\%$, where the passive contribution to aggregate F_{ANKLE} starts to increase to 4% of the origianl aggregate F_{PF}.

The normalized sums of activation profiles and metabolic costs when $K_{EXO} = 0\%$ to 97% $\vec{M}_{bio}$ K_t are plotted on Figure 3.6b. Both sums decrease roughly linearly until $K_{EXO} = \sim 88\%$ $\vec{M}_{bio}$ K_t, where they flatten. A careful observation shows that rate at which metabolic cost fell decreased slightly before increasing as K_{EXO} increased. Conversly, the aggregate activation declined at an increasingly negative rate before decreasing slightly prior to $K_{EXO} = 88\%$. At ~94%, both metabolic cost and activation profile sums begin to climb as the velocity of the CE

approaches $V_{CE_{MAX}}$ and necessitates maximal activation at 61% in the stride.

Figure 3.6c displays the total positive mechanical work performed by each element over the range of K_{EXO} values. W^{+}_{MTU} decreases linearly as the force requirements of the MTU are offset by the K_{EXO} contribution until it reaches a steady state at $K_{EXO} = 88\%\ \vec{M}_{bio}\ K_t$. W^{+}_{CE} seemed to asymptotically approach W^{+}_{MTU} until $K_{EXO} = 88\%$, where it also flattens.

Lastly, Figure 3.6d displays the metabolic cost estimate of the plantar flexors, an estimate of the compensatory metabolic cost that would be incurred by either the local (i.e the dorsiflexors) or global antagonist (i.e. muscles modulating the knee joint or hip joint), and the total estimated metabolic cost for the range of K_{EXO} values from 0% to 97% $K_{BIO}\ K_t$. Each metabolic cost estimate is normalized to the metabolic cost of K_{BIO}. The sum of the PF metabolic cost and compensatory metabolic cost (shown in blue) is minimized at $K_{EXO} = \sim 71\%$ of $K_{BIO}\ K_t$ with a total metabolic cost of 73% of the $\vec{M}_{bio}\ W_{met}$, or 36.7 J. The total metabolic cost is equal to the unassisted $\vec{M}_{bio}$ metabolic cost at ∼94%. Once again, past 94%, the metabolic cost begin to climb as the velocity of the CE approaches $V_{CE_{MAX}}$.

The time series data from select K_{EXO} values are shown in Figure 3.7 and Figure 3.8. In these figures, the activation profiles, element force profiles, mechanical power profiles, and metabolic power profiles are shown for $K_{EXO} = 0\%$, 20%, 50%, and 90% of $K_{BIO}\ K_t$. As K_{EXO} increases in magnitude, the activation profiles systemically decrease until a spike of activation occurs shortly after 61% of the stride (Figure 3.7a - d). An activation of 1 is equivalent to maximal CE activation. Figure 3.7a - d also show a delay in the onset of CE activation as K_{EXO} increases. The metabolic power profiles of the K_{EXO} solutions shown in Figure 3.8e - h follow the same trend as the the activation profiles, where metabolic powers systematically decrease and shift to further in the stride.

Figure 3.7e - h show the force traces of the select K_{EXO} solutions. Idealized F_{EXO} contribution, shown in solid black, gradually replaces the F_{ANKLE} profile betwen 9% and 60% of the stride. The light black traces in Figure 3.7f - h indicate where the F_{EXO} contribution exceeded the needed F_{PF}, and would have to be compensated for by antagonist muscles (i.e. tibialis anterior) to preserve m_{net}.

Figure 3.8a - d show the mechanical powers for the MTU, CE, and SEE as K_{EXO} varies from 0%(a) to 90%(d). As seen in Figure 3.6c, as K_{EXO} increases, the magnitudes of positive power generated by each element decreases until the CE performs the majority of W^{+}_{MTU} (~ 2 J). Additionally, the positive mechanical work performed by the CE is approximately equal in magnitude to the work performed by the SEE at $K_{EXO} = 0\%$, whereas with increased K_{EXO} values, the relative contribution of the CE W^{+}_{CE} steadily outpaces the SEE W^{+}_{SEE}.

Finally, Figure 3.9 displays the CE excursion that occurs as the biological tissue is unloaded by K_{EXO} for $K_{EXO} = 0\%$, 20%, 50%, and 90% of $K_{BIO}\ K_t$. While the strain pattern between 0 and $\sim 13\%$ of the stride as well as $> 60\%$ of the stride remain identical for all traces of K_{EXO},

CE excursion steadily increases as K_{EXO} increases. L_{CE} surpasses L_{CE_0} for the $K_{EXO} = 50$ % configuration between ∼32% and ∼50% of the stride with a max CE strain of ∼6%, while the $K_{EXO} = 90\%$ configuration induces an L_{CE} strain above 1 for points in the stride between ∼32% and ∼59% with a peak strain of ∼15%.

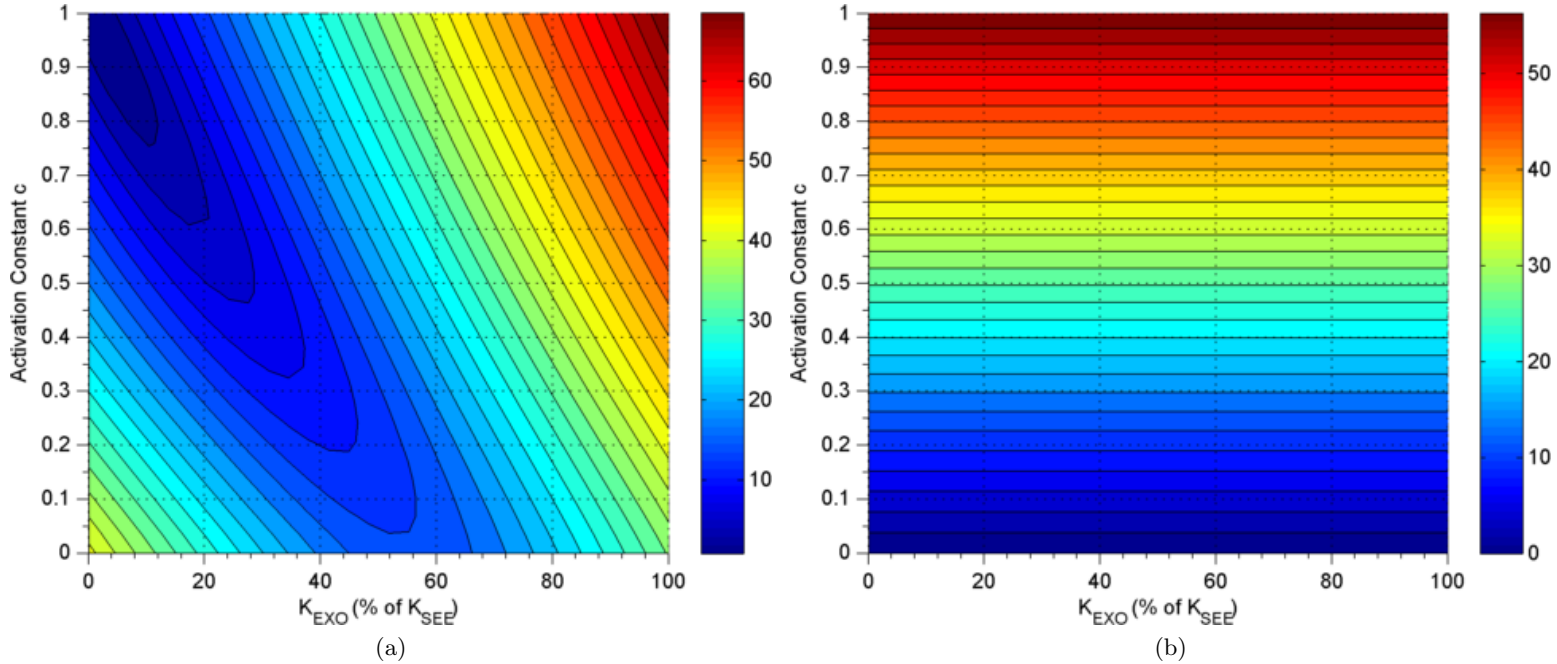

Figure 3.5: **Contour maps of RMSE and Metabolic Cost for $\vec{M}_{EXO}$ vector space.** a) RMSE of $\vec{M}_{EXO}$ vector space. The minimum RMSE exists at $\vec{M}_{EXO}$ = [0 (K_{EXO}),1 (c)]. While no other space on the contour produces an RMSE that matches [0,1], a linear 'valley' feature exists from [0,1] to [.60, 0]. b) Metabolic cost of $\vec{M}_{EXO}$ vector space. The metabolic cost of each solution depends entirely on the scaling factor c. The minimum metabolic cost lies trivially on the $c = 0$ line in vector space.

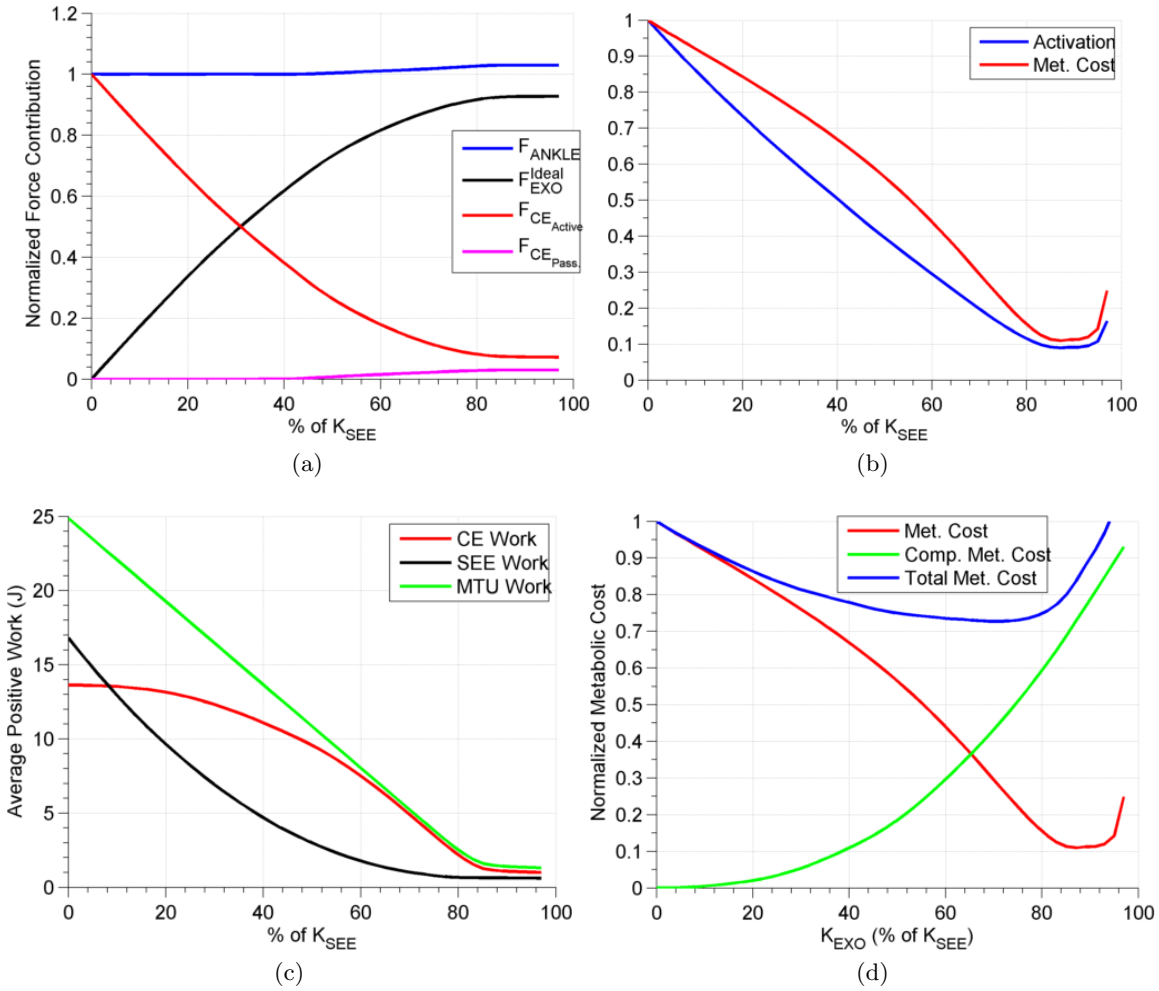

Figure 3.6: **Characterizations of force, activation, and power behaviors as K_{EXO} is varied from 0% to 100% of the K_{BIO} K_t.** Solutions do not resolve past ∼97% due to the CE $V_{CE_{MAX}}$ capacity being surpassed during the stride simulation. a) Aggregate ankle force, EXO force, active CE force, and passive CE force (normalized to the $\vec{M}_{bio}$ F_{PF} sum). b) Sums of Activation and metabolic cost (normalized to respective maximum values). c) Positive mechanical work performed by the MTU, SEE, CE across K_{EXO} values. d) Metabolic cost of PF, compensatory metabolic cost, and sum of the two estimates. The minimum total (i.e. plantar flexor and compensatory) metabolic cost occurs at K_{EXO} = ∼71% of K_{BIO} with a total cost of 73% of the $\vec{M}_{bio}$ W_{met}, or 36.7 J.

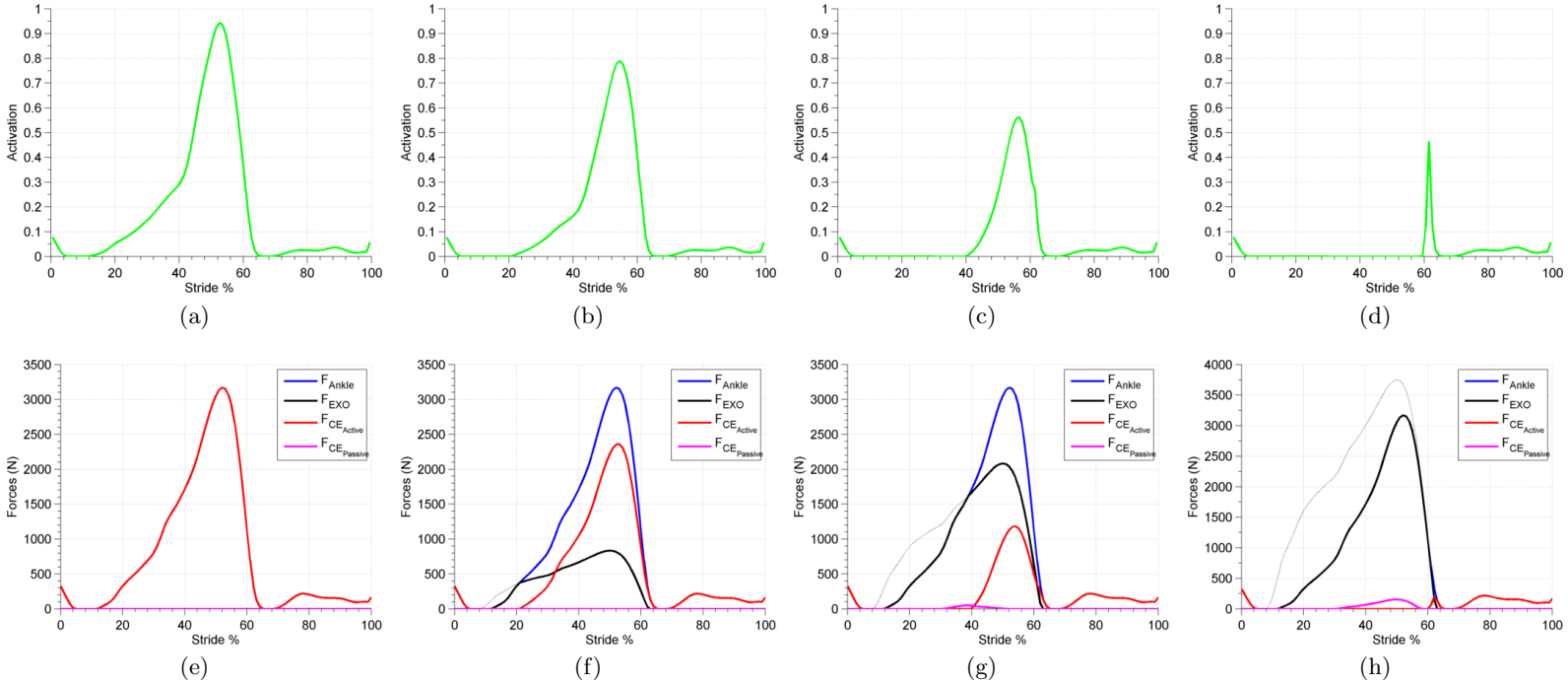

Figure 3.7: **Activation[top] and force profiles[bottom] for select K_{EXO} values.** a,e) Activation and force profiles for model with $K_{EXO} = 0\%$ of K_{BIO}. Peak activation was 95.3%. b,f) Activation and force profiles for model with $K_{EXO} = 20\%$ of K_{BIO}. Peak activation was 79.0%. c,g) Activation and forResultce profiles for model with $K_{EXO} = 50\%$ of K_{BIO}. Peak activation was 56.2%. d,h) Activation and force profiles for model with $K_{EXO} = 90\%$ of K_{BIO}. Peak activation was 46.4%. The thin black line on (f) through (h) indicates where F_{EXO} surpassed F_{PF} requirements, and would necessitate coactivation of the dorsiflexors to conserve a human plantar flexor moment profile.

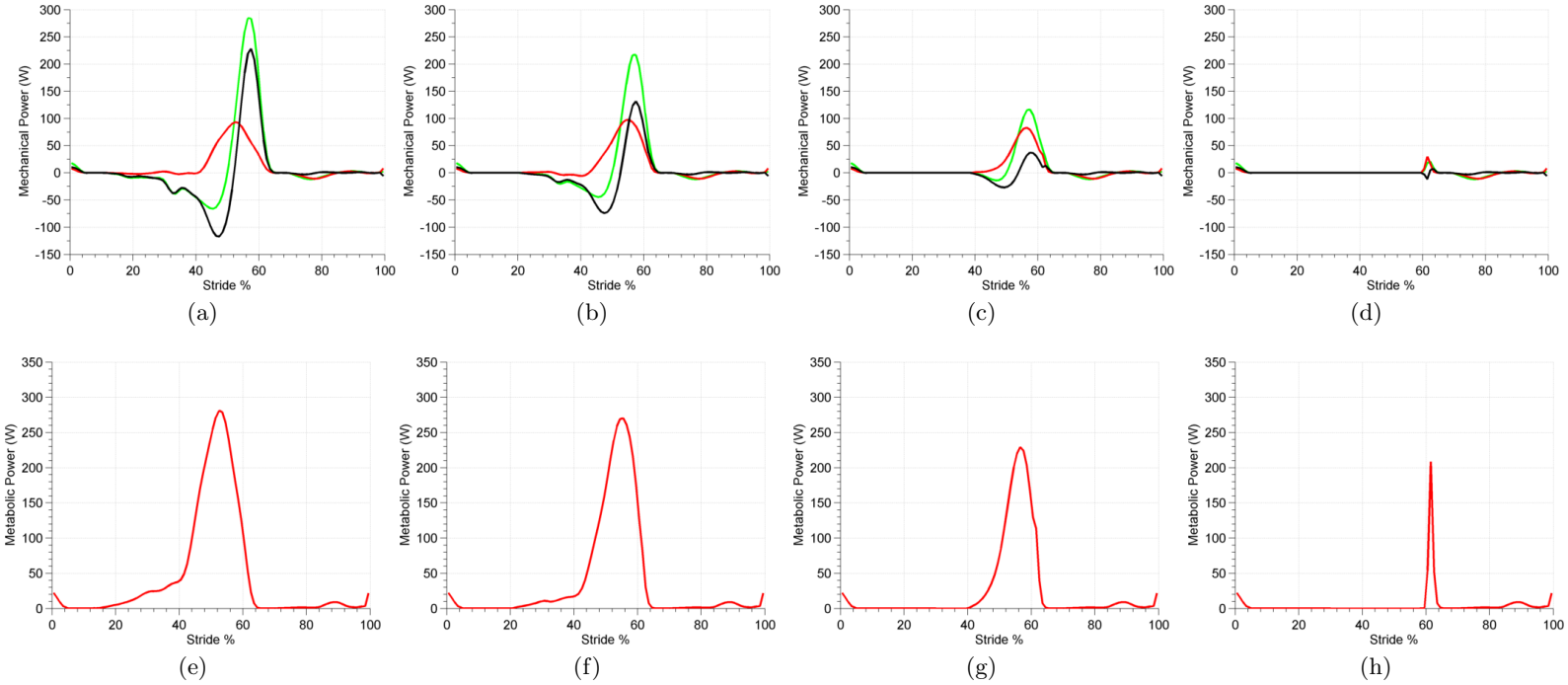

Figure 3.8: **Mechanical[top] and metabolic[bottom] power profiles for select K_{EXO} values.** The CE, SEE, and MTU mechanical power traces correspond to red, black, and green. a,e) Solution for $K_{EXO} = 0\%$ of K_{BIO}. $W^{+}_{CE} = 13.6$ J; Total metabolic cost was 50.3 J. b,f) Solution for $K_{EXO} = 20\%$ of K_{BIO}. $W^{+}_{CE} = 13.1$ J; Total metabolic cost was 41.6 J. c,g) Solution for $K_{EXO} = 50\%$ of K_{BIO}. $W^{+}_{CE} = 9.2$ J; Total metabolic cost was 27.9 J. d,h) Solution for $K_{EXO} = 90\%$ of K_{BIO}. $W^{+}_{CE} = 1.08$ J; Total metabolic cost was 5.52 J.

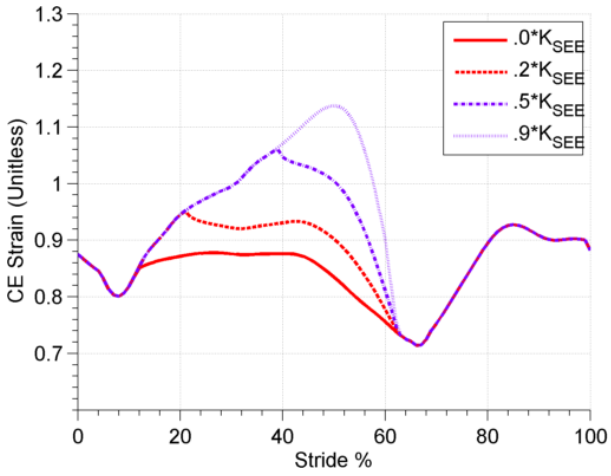

(a)

Figure 3.9: **CE Strain patterns for select K_{EXO} values.** CE strain patterns as elastic assistance K_{EXO} increased between 0%, 20%, 50%, and 90% of K_{BIO}.

3.4 Discussion

The goal of this study was to employ a simple, data-driven computational model of an elastic ankle exoskeleton working in parallel with the biological plantarflexors to determine how exoskeleton stiffness would influence the neuromechanics and energetics of the underlying muscle-tendon units during walking. We hypothesized that increasing exoskeleton stiffness would (1) lead to systematic decreases in metabolic energy consumption of the plantarflexors and (2) disrupt the normal catapult-like muscle-tendon interaction dynamics (i.e. nearly isometric muscle fascicles with large stretch and recoil of series elastic tissues) of the plantarflexors during walking. Our results supported both hypotheses.

As expected, stiffer ankle exoskeleton springs resulted in larger decreases in plantarflexor metabolic energy consumption. The metabolic cost of the plantarflexors depended entirely on muscle activation, and were independent of the exoskeleton stiffness, as indicated by perfectly horizontal metabolic cost contours in c - K_{EXO} space (Figure 3.5b). However, many of the c - K_{EXO} combinations resulted in total (exoskeleton + biological) ankle joint moments that greatly deviated from the normal pattern during walking without assistance (i.e. RMSE >>0) (Figure 3.5a). In fact, it was not possible to shut down the plantarflexors and exactly match the normal ankle joint moment with a stiff, linear exoskeleton spring. The RMSE in the ankle moment was $\sim$ 40 N-m for the 100% exoskeleton 0% biological contribution solution (Figure 3.5a, bottom left). Despite this limitation, it was possible to produce nearly normal total ankle joint moments by trading-off biological plantarflexor activation intensity (i.e. reducing c in $c \times \alpha(t)$)

with increasing K_{EXO} along a line in contour space spanning from c=1, K_{EXO} =0% K_t to c=0, K_{EXO} =60% K_t (Figure 3.5a). Along this path in parameter space, the metabolic cost of plantarflexion was reduced from 50.3 J to 0 J, per leg. In short, the model predicts that it should be possible to reduce the metabolic cost of plantarflexion to zero with an exoskeleton spring stiffness of 187 Nmm^{-1} attached at the calcaneus (187 Nmm^{-1} = 315 N-m/rad = 5.5 N-m/deg). Based on reported values for the metabolic cost of walking at 1.25 m/s (310 J net, or ∼400 J gross)[60], we estimate that reducing the metabolic cost of the plantarflexors to zero would equate to an overall reduction in the metabolic cost of walking of ∼25%. This is consistent with other published estimates of the relative contribution of the plantarflexors to total the metabolic cost of walking[60][62]. We highlight that the best solution possible by merely scaling plantarflexor activation (see Section 3.2.3) does not generate a normal ankle joint moment pattern (i.e. RMSE = ∼10 N-m) and may therefore require some compensation from antagonists at the ankle or muscle-tendons spanning other joints to maintain overall gait dynamics.

Humans seem to employ a motor control strategy in order to maintain invariant ankle joint moments during locomotion with mechanical assistance from exoskeletal devices[12][14][21][23][25][41]. In our forward modeling framework, we assumed that the human user could only adjust the magnitude of the plantarflexor activation pattern, but not the timing. This was intended to simulate short term neuronal adaptation that might occur early in learning[40]. However, neuronal adaptation may also involve changes in the timing of muscle activation[59]. Thus, to more accurately model kinetic invariance in humans, we expanded our framework to include solutions that enforced calculated plantarflexor contribution to joint moment and angle during walking at 1.25 ms^{-1}(i.e. kinetic and kinematic invariant solutions, see Section 3.2.3) (Figure 3.6 - Figure 3.9). Not surprisingly, as exoskeleton spring stiffness (K_{EXO}) increased, the $\vec{M}_{bio}\ m_{PF}$ that conserved m_{net} required a muscle activation with lesser magnitude *and* at a later onset. Without this timing shift, the muscle (CE) would have produced unnecessary force between ∼10% and 60% of the stride when exoskeleton assistance F_{EXO} was already sufficient (Figure 3.7).

In line with the forward framework results, solutions with kinetic invariance demonstrate that increasing K_{EXO} yields a clear trade-off between exoskeleton and biological muscle forces, with a ∼50/50% sharing at K_{EXO} of ∼30% K_t (= 158 N-m/rad = 2.8N-m/deg) (Figure 3.6a). In line with our hypothesis, as the biological force requirement declines with increasing K_{EXO}, so does muscle activation, which is the main driver of metabolic cost. Metabolic cost of the plantarflexors reaches a minimum value of ∼11% of the value during unassisted walking (50.3 J *0.11 = 5.5 J per leg) with a K_{EXO} of ∼80% K_t (= 421 N-m/rad = 7.4 N-m/deg) (Figure 3.6b). Interestingly, assisting with a $K_{EXO} \geq 45\%\ K_t$ induced passive stretch in the muscle fascicles (CE) and a small passive muscle moment contribution. This elicited an unavoidable deviation

in the ankle moment profile from normal walking (Figure 3.6a, purple; and Figure 3.7g - h). Thus, due to shifts in the operating point of underlying muscles to longer lengths (Figure 3.9), perfectly conserving the m_{PF} may become increasingly difficult, and could be a factor that limits performance for exoskeletons employing high parallel stiffness[12].

If humans choose to move with very strict ankle moment invariance, they may reject exoskeletons with stiffness $\geq$50% K_t (or $\sim$60% of normal ankle joint rotational stiffness during walking at 1.25 ms^{-1}[61]). This could severely limit the potential for metabolic savings to only $\sim$60% of the total plantarflexor contribution (Figure 3.6c), or $\sim$15% overall. In addition, solutions with K_{EXO} $\geq$50% K_t begin to significantly produce excess exoskeleton moments early in the stance phase (Figure 3.7f - h; thin black). To maintain ankle moment invariance, these excess moments would need to be countered by significant forces in the ankle dorsiflexors or adjustments in posture, both of which incurring metabolic cost(Figure 3.6d). Thus, a 15% reduction in metabolic cost of walking may be a high end estimate.

Despite the potential for significant metabolic savings due to reduced muscle forces and activations (Figure 3.6a, b), our results also support the hypothesis that elastic ankle exoskeletons could significantly disrupt the normal catapult action of the plantarflexors during human walking. Our model with K_{EXO} = 0% K_{BIO} captures the normal muscle-tendon interaction dynamics of the plantarflexors and Achilles tendon during walking (Khan et al., Chapter 2)[42], with nearly isometric muscle fascicles during stance phase (Figure 3.9, red) and large amounts of elastic energy storage and return in series elastic tissues.This results in a large burst of mechanical power at push-off that is shared 50/50 between muscle fascicles (CE) and series elastic tissues (SEE) (Figure 3.6c, Figure 3.8a). However, as K_{EXO} increases, unloading of the biological MTU causes less and less stretch in the SEE and more and more stretch in the CE, disrupting the normal catapult-like muscle-tendon interaction(Figure 3.6c).

Our prediction that the CE undergoes larger excursions with parallel mechanical assistance is consistent with recent muscle-level experiments during spring-loaded human hopping. Soleus fascicles undergo increased excursions in the presence of a parallel spring (K_{EXO} = 91 N-m/rad) providing assistive plantarflexor torque[21]. In that case, reduced forces were counteracted by increased length changes resulting in no difference in soleus muscle fascicle work between spring-loaded and unassited hopping conditions. Our model of spring-loaded walking makes a similar prediction that CE work does not decrease for values of K_{EXO} up to $\sim$20% K_t (= 105 N-m/rad = 1.8 N-m/rad)(Figure 3.6c). For stiffness values >20% K_t, CE work begins to decline as reductions in muscle force outpace increases in CE length changes. Perhaps more striking is the rapid reduction in the mechanical work performed by SEE recoil with increasing exoskeleton spring stiffness. Without assistance from the exoskeleton, the SEE recoil contributes an equal amount of mechanical power as CE shortening, but the SEE contribution is reduced to nearly zero for $K_{EXO} \geq$ 70% K_t, completely eliminating the ability of the biological MTU to function

as a catapult(Figure 3.6c).

Increasing reliance on the CE for MTU power production limits the metabolic benefit of increasing exoskeleton spring stiffness. The lack of mechanical power from elastic recoil of the SEE is mostly supplanted by elastic recoil of the exoskeleton spring, but not without some consequence. Our metabolic cost model is driven by both muscle activation and muscle velocity[2](Eq. 2.14). As exoskeleton spring stiffness increases, the required muscle activation declines because biological muscle force requirements are reduced. We note, however, that reductions in metabolic cost occur at a slower rate than reductions in muscle activation (Figure 3.6b). This is a direct side effect of the metabolic penalty associated with the higher CE shortening velocities due to the increased muscle excursions characteristic of a disrupted catapult action(Figure 3.9). Thus, in general, it would seem that exoskeletons designed to assist MTUs with compliant architecture may be inherently limited in their metabolic benefit. One way out of this conundrum might be for the user to adjusts their joint kinematics (and therefore MTU length change pattern) in order to attenuate increases in underlying fascicle velocity that counteract the metabolic reductions due to reduced muscle forces and activations[21]. Indeed, altered joint kinematics indicative of shorter MTU lengths (i.e. exaggerated plantarflexion) have been observed during walking with powered ankle orthoses[40][52][59] - a strategy that may limit metabolic penalty due to a disrupted catapult mechanism.

Aside from improving metabolic performance of the user, exaggerated plantar flexion during walking with an ankle exoskeleton could be indicative of an injury avoidance mechanism. Although non-intuitive, walking with relatively stiff exoskeleton springs could induce passive stretch at high rates in the CE and increase the likelihood of a muscle strain injury[28]. In our simulations, the CE strain reached maximum values of $\sim$115% for the stiffest exoskeleton spring (Figure 3.9), but for tasks where the MTU operates at longer lengths and/or faster velocities (e.g. faster walking or walking uphill), it is possible that strains/strain rates might reach dangerous levels with relatively stiff exoskeletons (e.g. $K_{EXO} > 90\%\ K_t$ or 475 N-m/rad).

3.4.1 Model Limitations

We made a number of simplifications and assumptions in developing the model and simulations used in this study that are worth addressing. First and foremost, we greatly simplified the attachment geometry, muscle-tendon architecture, and mechanisms driving force production in our musculoskeletal model of the triceps surae (i.e. medial gastrocnemius, lateral gastrocnemius and soleus), the details and limitations of which have been addressed previously (Khan et al., Chapter 2)[42]. Briefly, we combined the triceps surae group into a single, lumped uniarticular muscle-tendon with a soleus like origin and insertion locations, but with a force generating capacity of the summed MG + LG + SOL. Despite its simplicity, we believe the model captures

all of the features and behaviors exhibited by the human plantar flexors during walking that are relevant to the questions we address in this study.

The inverse modeling framework we employed assumed that the overall ankle joint kinematics and kinetics remain invariant in the context of elastic ankle exoskeletons. While there is strong evidence that humans do indeed exhibit invariance in ankle joint moments during walking [13][41], the evidence for ankle joint angle invariance is weak. For example, Kao et al. demonstrated that, while ankle kinetics are conserved when some plantar flexor moment is provided by a robotic exoskeleton, ankle kinematics tend to shift to more plantarflexed postures[41]. This finding has been corroborated by others who use ankle exoskeletons during human walking studies[52]. We note that it is entirely possible that the devices used in previous studies were not properly 'tuned' to reproduce both ankle kinetics and kinematics during the studied gait pattern. In fact, our study strongly suggests that assistive devices that are not properly 'tuned' could lead to deviations from normal moments without significant adjustment in joint kinematics and/or muscle activation patterns(Figure 3.7e - h). As such, we believe our study informs the end goal of ideal mechanical assistance, where the natural walking pattern is maintained in the context of localized mechanical assistance.

3.4.2 Insights into Improving Current Ankle Exoskeleton Designs

In this study, we have highlighted a number of limitations inherent in passive elastic exoskeleton designs[66] that may be overcome with improvements in future designs. The primary drawback to the device we simulated was that it produced forces early in the stance phase that often exceeded those needed to produce a normal ankle joint moment. This effect was particularly noticible as the exoskeleton spring stiffness increased (Figure 3.7e - h). With the current design, avoiding this excess exoskeleton moment would require either (a) a change in ankle joint kinematics; or (b) co-activation by ankle dorsiflexors to adjust the net ankle moment downward; or (c) walking with excessive total ankle joint moments - all of which are undesirable effects. Changes in the exoskeleton design could also improve performance. For example, a passive device with non-linear spring stiffness (i.e. a stiffening spring), and/or a changing moment arm could be designed with a custom torque angle curve appropriate for a given gait. In addition, timing engagement of the spring with a more versatile clutching mechanism could provide flexibility in when the exoskeleton torque onset occurs during a gait cycle. Of course, a device with motors could achieve all of the aforementioned performance features by employing customized gait-phase dependent torque control that is optimized to maximize metabolic benefit while maintaining joint kinetics and kinematics.

Finally, we note that our results suggest that, for devices intended to reduce metabolic cost of human locomotion by assisting compliant joints (e.g. ankle), the name of the game is to reduce

muscle forces and activations. This idea represents somewhat of a paradigm shift from previous solutions focusing on reducing the biological muscle-tendon/ joint positive mechanical power outputs[52][59]. It may be that passive elastic solutions may be better suited for reducing muscle activations over a gait cycle, as they can reduce the force requirements in a parallel biological muscle-tendon unit even during periods of energy absorption.

REFERENCES

[1] Albracht, K., and Arampatzis, A. Exercise-induced changes in triceps surae tendon stiffness and muscle strength affect running economy in humans. *European journal of applied physiology 113*, 6 (2013), 1605–1615.

[2] Alexander, R. M. Optimum muscle design for oscillatory movements. *Journal of theoretical biology 184*, 3 (2/7 1997), 253–259.

[3] Alexander, R. M., and Ker, R. *The architecture of leg muscles.* Multiple muscle systems. Springer, 1990, pp. 568–577.

[4] Arampatzis, A., Stafilidis, S., DeMonte, G., Karamanidis, K., Morey-Klapsing, G., and Brggemann, G. Strain and elongation of the human gastrocnemius tendon and aponeurosis during maximal plantarflexion effort. *Journal of Biomechanics 38*, 4 (2005), 833–841.

[5] Arnold, E. M., and Delp, S. L. Fibre operating lengths of human lower limb muscles during walking. *Philosophical Transactions of the Royal Society B: Biological Sciences 366*, 1570 (2011), 1530–1539.

[6] Arnold, E. M., Hamner, S. R., Seth, A., Millard, M., and Delp, S. L. How muscle fiber lengths and velocities affect muscle force generation as humans walk and run at different speeds. *The Journal of experimental biology 216*, 11 (2013), 2150–2160.

[7] Arnold, E. M., Ward, S. R., Lieber, R. L., and Delp, S. L. A model of the lower limb for analysis of human movement. *Annals of Biomedical Engineering 38*, 2 (2010), 269–279.

[8] Azizi, E., Brainerd, E. L., and Roberts, T. J. Variable gearing in pennate muscles. *Proceedings of the National Academy of Sciences 105*, 5 (2008), 1745–1750.

[9] Biewener, A. A., and Roberts, T. J. Muscle and tendon contributions to force, work, and elastic energy savings: a comparative perspective. *Exercise and sport sciences reviews 28*, 3 (2000), 99–107.

[10] Blickhan, R. The spring-mass model for running and hopping. *Journal of Biomechanics 22*, 11 (1989), 1217–1227.

[11] Brand, R. A., Crowninshield, R. D., Wittstock, C. E., Pedersen, D. R., Clark, C. R., and van Krieken, F. M. A model of lower extremity muscular anatomy. *Journal of Biomechanical Engineering 104*, 4 (Nov 1982), 304–310. LR: 20071114; GR: AM1 4486/AM/NIADDK NIH HHS/United States; JID: 7909584; ppublish.

[12] Bregman, D., Harlaar, J., Meskers, C., and de Groot, V. Spring-like ankle foot orthoses reduce the energy cost of walking by taking over ankle work. *Gait and posture 35*, 1 (2012), 148–153.

[13] Bregman, D., Van der Krogt, M., De Groot, V., Harlaar, J., Wisse, M., and Collins, S. The effect of ankle foot orthosis stiffness on the energy cost of walking: A simulation study. *Clinical Biomechanics 26*, 9 (2011), 955–961.

[14] Chang, Y.-H., Roiz, R. A., and Auyang, A. G. Intralimb compensation strategy depends on the nature of joint perturbation in human hopping. *Journal of Biomechanics 41*, 9 (2008), 1832–1839.

[15] Cherry, M. S., Choi, D. J., Deng, K. J., Kota, S., and Ferris, D. P. Design and fabrication of an elastic knee orthosis: preliminary results. ASME.

[16] Chleboun, G. S., Busic, A. B., Graham, K. K., and Stuckey, H. A. Fascicle length change of the human tibialis anterior and vastus lateralis during walking. *The Journal of orthopaedic and sports physical therapy 37*, 7 (2007), 372.

[17] Daley, M., Felix, G., and Biewener, A. Running stability is enhanced by a proximo-distal gradient in joint neuromechanical control. *Journal of Experimental Biology 210*, 3 (2007), 383–394.

[18] de Zee, M., and Voigt, M. Moment dependency of the series elastic stiffness in the human plantar flexors measured in vivo. *Journal of Biomechanics 34*, 11 (2001), 1399–1406.

[19] Elliott, G., Sawicki, G. S., Marecki, A., and Herr, H. The biomechanics and energetics of human running using an elastic knee exoskeleton.

[20] Farley, C. T., Blickhan, R., Saito, J., and Taylor, C. R. Hopping frequency in humans: a test of how springs set stride frequency in bouncing gaits. *Journal of applied physiology 71*, 6 (1991), 2127–2132.

[21] Farris, D. J., Robertson, B. D., and Sawicki, G. S. Elastic ankle exoskeletons reduce soleus muscle force but not work in human hopping. *Journal of applied physiology* (2013).

[22] Farris, D. J., and Sawicki, G. S. Human medial gastrocnemius forcevelocity behavior shifts with locomotion speed and gait. *Proceedings of the National Academy of Sciences 109*, 3 (2012), 977–982.

[23] Farris, D. J., and Sawicki, G. S. Linking the mechanics and energetics of hopping with elastic ankle exoskeletons. *Journal of applied physiology 113*, 12 (December 15 2012), 1862–1872.

[24] Farris, D. J., and Sawicki, G. S. The mechanics and energetics of human walking and running: a joint level perspective. *Journal of the Royal Society, Interface / the Royal Society 9*, 66 (Jan 7 2012), 110–118. LR: 20130524; JID: 101217269; OID: NLM: PMC3223624; 2011/05/25 [aheadofprint]; ppublish.

[25] Ferris, D. P., Bohra, Z. A., Lukos, J. R., and Kinnaird, C. R. Neuromechanical adaptation to hopping with an elastic ankle-foot orthosis. *Journal of applied physiology 100*, 1 (2006), 163–170.

[26] Ferris, D. P., Gordon, K. E., Sawicki, G. S., and Peethambaran, A. An improved powered ankle-foot orthosis using proportional myoelectric control. *Gait and posture 23*, 4 (Jun 2006), 425–428. LR: 20071114; GR: NS045486/NS/NINDS NIH HHS/United States; JID: 9416830; 2004/10/11 [received]; 2005/01/17 [revised]; 2005/05/01 [accepted]; 2005/08/10 [aheadofprint]; ppublish.

[27] Fukunaga, T., Kubo, K., Kawakami, Y., Fukashiro, S., Kanehisa, H., and Maganaris, C. N. In vivo behaviour of human muscle tendon during walking. *Proceedings of the Royal Society of London.Series B: Biological Sciences 268*, 1464 (2001), 229–233.

[28] Garrett, W. E., J. Muscle strain injuries: clinical and basic aspects. *Medicine and science in sports and exercise 22*, 4 (Aug 1990), 436–443. LR: 20051116; JID: 8005433; RF: 62; ppublish.

[29] Geyer, H., and Herr, H. A muscle-reflex model that encodes principles of legged mechanics produces human walking dynamics and muscle activities. *Neural Systems and Rehabilitation Engineering, IEEE Transactions on 18*, 3 (2010), 263–273.

[30] Geyer, H., Seyfarth, A., and Blickhan, R. Compliant leg behaviour explains basic dynamics of walking and running. *Proceedings of the Royal Society B: Biological Sciences 273*, 1603 (2006), 2861–2867.

[31] Gordon, K. E., Sawicki, G. S., and Ferris, D. P. Mechanical performance of artificial pneumatic muscles to power an ankle-foot orthosis. *Journal of Biomechanics 39*, 10 (2006), 1832–1841. LR: 20091111; GR: R01NS045486/NS/NINDS NIH HHS/United States; JID: 0157375; 2004/12/08 [received]; 2005/05/20 [accepted]; 2005/07/14 [aheadofprint]; ppublish.

[32] Gottschall, J. S., and Kram, R. Energy cost and muscular activity required for propulsion during walking. *Journal of applied physiology 94*, 5 (2003), 1766–1772.

[33] Grabowski, A. M., and Herr, H. M. Leg exoskeleton reduces the metabolic cost of human hopping. *Journal of applied physiology 107*, 3 (2009), 670–678.

[34] Hawkins, D., and Hull, M. L. A method for determining lower extremity muscle-tendon lengths during flexion/extension movements. *Journal of Biomechanics 23*, 5 (1990), 487–494. LR: 20091111; JID: 0157375; ppublish.

[35] Hill, A. The heat of shortening and the dynamic constants of muscle. *Proceedings of the Royal Society of London.Series B, Biological Sciences 126*, 843 (1938), 136–195.

[36] Hof, A. *in vivo* measurement of the series elasticity release curve of human triceps surae muscle. *Journal of Biomechanics 31*, 9 (1998), 793–800.

[37] Hof, A., Van Zandwijk, J., and Bobbert, M. Mechanics of human triceps surae muscle in walking, running and jumping. *Acta Physiologica Scandinavica 174*, 1 (2002), 17–30.

[38] Houghton, L., Dawson, B., and Rubenson, J. Achilles tendon mechanical properties after both prolonged continuous running and prolonged intermittent shuttle running (cricket batting). *Journal of applied biomechanics* (Aug 22 2012). JID: 9315240; aheadofprint.

[39] Ishikawa, M., Komi, P. V., Grey, M. J., Lepola, V., and Bruggemann, G.-P. Muscle-tendon interaction and elastic energy usage in human walking. *Journal of applied physiology 99*, 2 (2005), 603–608.

[40] Kao, P.-C., Lewis, C., and Ferris, D. Short-term locomotor adaptation to a robotic ankle exoskeleton does not alter soleus hoffmann reflex amplitude. *Journal of NeuroEngineering and Rehabilitation 7*, 1 (2010), 33. M3: 10.1186/1743-0003-7-33.

[41] Kao, P.-C., Lewis, C. L., and Ferris, D. P. Invariant ankle moment patterns when walking with and without a robotic ankle exoskeleton. *Journal of Biomechanics 43*, 2 (2010), 203–209.

[42] Khan, N. S. A data-driven muscle-tendon modeling framework to evaluate muscle-level performance of ankle exoskeletons during human walking, 2013.

[43] Krishnaswamy, P., Brown, E. N., and Herr, H. M. Human leg model predicts ankle muscle-tendon morphology, state, roles and energetics in walking. *PLoS computational biology 7*, 3 (Mar 2011), e1001107. LR: 20130524; GR: DP1 OD003646/OD/NIH HHS/United States; JID: 101238922; OID: NLM: PMC3060164; 2010/08/16 [received]; 2011/02/10 [accepted]; 2011/03/17 [epublish]; ppublish.

[44] Lagarias, J. C., Reeds, J. A., Wright, M. H., and Wright, P. E. Convergence properties of the nelder–mead simplex method in low dimensions. *SIAM Journal on Optimization 9*, 1 (1998), 112–147.

[45] Lichtwark, G. A., and Wilson, A. M. In vivo mechanical properties of the human achilles tendon during one-legged hopping. *The Journal of experimental biology 208*, Pt 24 (Dec 2005), 4715–4725. LR: 20061115; JID: 0243705; ppublish.

[46] Lichtwark, G. A., and Wilson, A. M. Is achilles tendon compliance optimised for maximum muscle efficiency during locomotion? *Journal of Biomechanics 40*, 8 (2007), 1768–1775. LR: 20091111; JID: 0157375; 2006/05/12 [received]; 2006/07/31 [accepted]; 2006/11/13 [aheadofprint]; ppublish.

[47] Lichtwark, G. A., and Wilson, A. M. Optimal muscle fascicle length and tendon stiffness for maximising gastrocnemius efficiency during human walking and running. *Journal of theoretical biology 252*, 4 (Jun 21 2008), 662–673. LR: 20081121; GR: Biotechnology and Biological Sciences Research Council/United Kingdom; JID: 0376342; 2007/08/09 [received]; 2008/01/17 [revised]; 2008/01/23 [accepted]; 2008/01/31 [aheadofprint]; ppublish.

[48] Lichtwark, G. A., and Wilson, A. M. Optimal muscle fascicle length and tendon stiffness for maximising gastrocnemius efficiency during human walking and running. *Journal of theoretical biology 252*, 4 (Jun 21 2008), 662–673. LR: 20081121; GR: Biotechnology

and Biological Sciences Research Council/United Kingdom; JID: 0376342; 2007/08/09 [received]; 2008/01/17 [revised]; 2008/01/23 [accepted]; 2008/01/31 [aheadofprint]; ppublish.

[49] Maganaris, C. N., Baltzopoulos, V., and Sargeant, A. J. Changes in the tibialis anterior tendon moment arm from rest to maximum isometric dorsiflexion: in vivo observations in man. *Clinical Biomechanics 14*, 9 (1999), 661–666.

[50] Magnusson, S., Hansen, P., Aagaard, P., Brnd, J., DyhrePoulsen, P., Bojsen-Moller, J., and Kjaer, M. Differential strain patterns of the human gastrocnemius aponeurosis and free tendon, in vivo. *Acta Physiologica Scandinavica 177*, 2 (2003), 185–195.

[51] Magnusson, S. P., Aagaard, P., Rosager, S., Dyhre-Poulsen, P., and Kjaer, M. Loaddisplacement properties of the human triceps surae aponeurosis in vivo. *The Journal of physiology 531*, 1 (2001), 277–288.

[52] Malcolm, P., Derave, W., Galle, S., and De Clercq, D. A simple exoskeleton that assists plantarflexion can reduce the metabolic cost of human walking. *PloS one 8*, 2 (2013), e56137.

[53] McMahon, T. A., and Cheng, G. C. The mechanics of running: how does stiffness couple with speed? *Journal of Biomechanics 23* (1990), 65–78.

[54] McNeill Alexander, R. Tendon elasticity and muscle function. *Comparative Biochemistry and Physiology-Part A: Molecular and Integrative Physiology 133*, 4 (2002), 1001–1011.

[55] Neptune, R. R., and Sasaki, K. Ankle plantar flexor force production is an important determinant of the preferred walk-to-run transition speed. *Journal of Experimental Biology 208*, 5 (2005), 799–808.

[56] Roberts, T. J. The integrated function of muscles and tendons during locomotion. *Comparative Biochemistry and Physiology-Part A: Molecular and Integrative Physiology 133*, 4 (2002), 1087–1099.

[57] Roberts, T. J., and Azizi, E. Flexible mechanisms: the diverse roles of biological springs in vertebrate movement. *The Journal of experimental biology 214*, Pt 3 (Feb 1 2011), 353–361.

[58] Rubenson, J., Pires, N. J., Loi, H. O., Pinniger, G. J., and Shannon, D. G. On the ascent: the soleus operating length is conserved to the ascending limb of the force-length curve across gait mechanics in humans. *The Journal of experimental biology 215*, Pt 20 (Oct 15 2012), 3539–3551. JID: 0243705; 2012/07/05 [aheadofprint]; ppublish.

[59] Sawicki, G. S., and Ferris, D. P. Mechanics and energetics of level walking with powered ankle exoskeletons. *Journal of Experimental Biology 211*, 9 (2008), 1402–1413.

[60] Sawicki, G. S., Lewis, C. L., and Ferris, D. P. It pays to have a spring in your step. *Exercise and sport sciences reviews 37*, 3 (2009), 130.

[61] Shamaei, K., Sawicki, G. S., and Dollar, A. M. Estimation of quasi-stiffness and propulsive work of the human ankle in the stance phase of walking. *PloS one 8*, 3 (2013), e59935.

[62] Umberger, B. R. Stance and swing phase costs in human walking. *Journal of the Royal Society, Interface / the Royal Society 7*, 50 (Sep 6 2010), 1329–1340. LR: 20130529; JID: 101217269; OID: NLM: PMC2894890; 2010/03/31 [aheadofprint]; ppublish.

[63] Umberger, B. R., and Rubenson, J. Understanding muscle energetics in locomotion: New modeling and experimental approaches. *Exercise and sport sciences reviews 39*, 2 (2011), 59–67.

[64] Ward, S. R., Eng, C. M., Smallwood, L. H., and Lieber, R. L. Are current measurements of lower extremity muscle architecture accurate? *Clinical orthopaedics and related research 467*, 4 (Apr 2009), 1074–1082. LR: 20100921; GR: HD048501/HD/NICHD NIH HHS/United States; GR: HD050837/HD/NICHD NIH HHS/United States; JID: 0075674; OID: NLM: PMC2650051; 2008/02/22 [received]; 2008/10/10 [accepted]; 2008/10/30 [aheadofprint]; ppublish.

[65] Wickiewicz, T. L., Roy, R. R., Powell, P. L., and Edgerton, V. R. Muscle architecture of the human lower limb. *Clinical orthopaedics and related research (179)*, 179 (Oct 1983), 275–283. LR: 20071114; GR: 5-507RR7009-13/RR/NCRR NIH HHS/United States; GR: NS16333/NS/NINDS NIH HHS/United States; JID: 0075674; OID: NASA: 84003030; ppublish.

[66] Wiggin, M. B., Sawicki, G. S., and Collins, S. H. An exoskeleton using controlled energy storage and release to aid ankle propulsion. In *Rehabilitation Robotics (ICORR), 2011 IEEE International Conference on* (2011), IEEE, pp. 1–5.

[67] Zajac, F. E. Muscle and tendon: properties, models, scaling, and application to biomechanics and motor control. *Critical Reviews in Biomedical Engineering 17*, 4 (1989), 359–411. LR: 20071114; GR: NS 17662/NS/NINDS NIH HHS/United States; JID: 8208627; RF: 177; ppublish.

APPENDIX

Appendix A

Supplemental Information

A.1 LG, MG, SOL, and Lump MTU Profile Comparison

Part of the our study's motivation for characterizing plantarflexor function was to inform the design of wearable exoskeltons for the lower limb. Since current iterations of ankle exoskeletons are primarily uniartucular[25][26][31][59], we decided to model all three of the triceps surae group as a singular, blended muscle. Although this framework may enable results from our study to be more easily integrated into assistive exoskeletal designs, it's reductive approach to plantar flexor MTUs differs significantly with the biological system within the posterior compartment of the human lower limb.

The length of a given muscle-tendon unit(MTU) is dependent on where the MTU originates and inserts on the body. Though all three triceps surae MTUs(SOL, MG, and LG) insert into the calcaneal tuberosity of the talus, the MG and LG originate on the posterior aspect of the femoral condyles, while the SOL originates roughly 25% distally from the tibial condyles[34][11]. Our lump model did not directly emulate any of these muscles, and instead used a unique MTU origin. While the lump model conserved an insertion into the calcaneous, the origin was placed 12.5% distally from the tibial condyles. This placement was meant to be a compromise between the SOL and LG/MG group origins while still retaining the intended uniarticular configuration.

MTU profiles for the LG, MG, and SOL were produced for comparison in Figure A.1 using the same kinematics that were used for the lump model to illustrate differences in both absolute lengths and changes in lengths between traditionally configured muscles and the lump model muscle . While the lump model and SOL only required the ankle profile due to their unarticular configuration, the LG and MG were also modulated using the knee angle profile taken from the same study as the ankle[59](Figure A.1a). MTU regression equations developed by Hawkins and Hull[34], based on the insertion and origin estimates from Brand et al.[11], were used to establish the comparison. Because the Hawkins and Hull equations produce length profiles normalized

to the rigid segment that the muscle traverses, each regression profile was multiplied by the simulated shank length of .40 m inspired by Ward[64] for the lump model(Table 2.2).

The absolute lengths of the SOL, MG, LG, and lump were dramatically different (Figure A.1a) due to the differences in origin for each of the compared muscles. However, the similar change in lengths between muscles, particularly the SOL and Lump, indicates that the moment arm and origin used in the lump model were consistent with widely utilized biomechanics models (Figure A.1b). The variation between the uniarticular MTU's and the biarticular MTU's change in lengths can be explained by the flexion of the knee joint that occured shortly after push-off. Importantly, the knee flexion that begins around 45% of the stride caused the biarticular muscles to reach their peak MTU lengths prior to the peaks of the uniarticular muscles configurations (Figure A.1c). This may help explain the overproduction of moment in the $\vec{M}_{abs}$ and $\vec{M}_{abs}$ solution when compared to the m_{net}; without the inclusion of biarticular muscles that delivered force in sync with the m_{net} peak, it was impossible to precisely recreate a peak moment that matches the m_{net} profile.

A.2 RMSE Penalty Selection

Moment Profile Feature Corroboration The modeling framework in this study assumed that the CE profile taken from Rubenson et al. would adequately represent the triceps surae enough to produce a moment profile with accurate plantar flexion features. However, there was no method of indicating whether the optimum solution produced when enforcing the CE profile was an accurate representation of a human walking plantar flexor moment. Though some of the general behaviors predicted by the $\vec{M}_{bio}$ solution were corroberated by experimental results (see Section 2.4.1 for details) and suggest a plausible plantarflexor morphology for human walking, measures like W_{CE}^{+} and W_{met} would not necessarily be sensitive to small deviations in plantarflexor moment. It was therefore necessary to produce a method to validate optimal moment profiles features produced by conserving the SOL CE length profile.

The plantar flexor moment must be equal to or more positive than the m_{net} profile. Since there is no data with direct measurements of the plantar flexor moments throughout a given gait pattern, it is impossible alone to discern where the plantar flexors are equal to the m_{net} profile and where it exceeds it. For this reason, an alternative approach was taken to validate general features in the plantar flexor moment created by the Rubenson CE strain pattern and the lump MTU profile.

Tibialis Anterior Coactivation A model was created to estimate the dorsiflexion moment. The average fascicle length profile and the EMG profile of the tibialis anterior(TA) were digitized from data by Chleboun et al. (n=9; height=1.74 cm; Walking speed = 1.3 ms^{-1})[16]. The fascicle

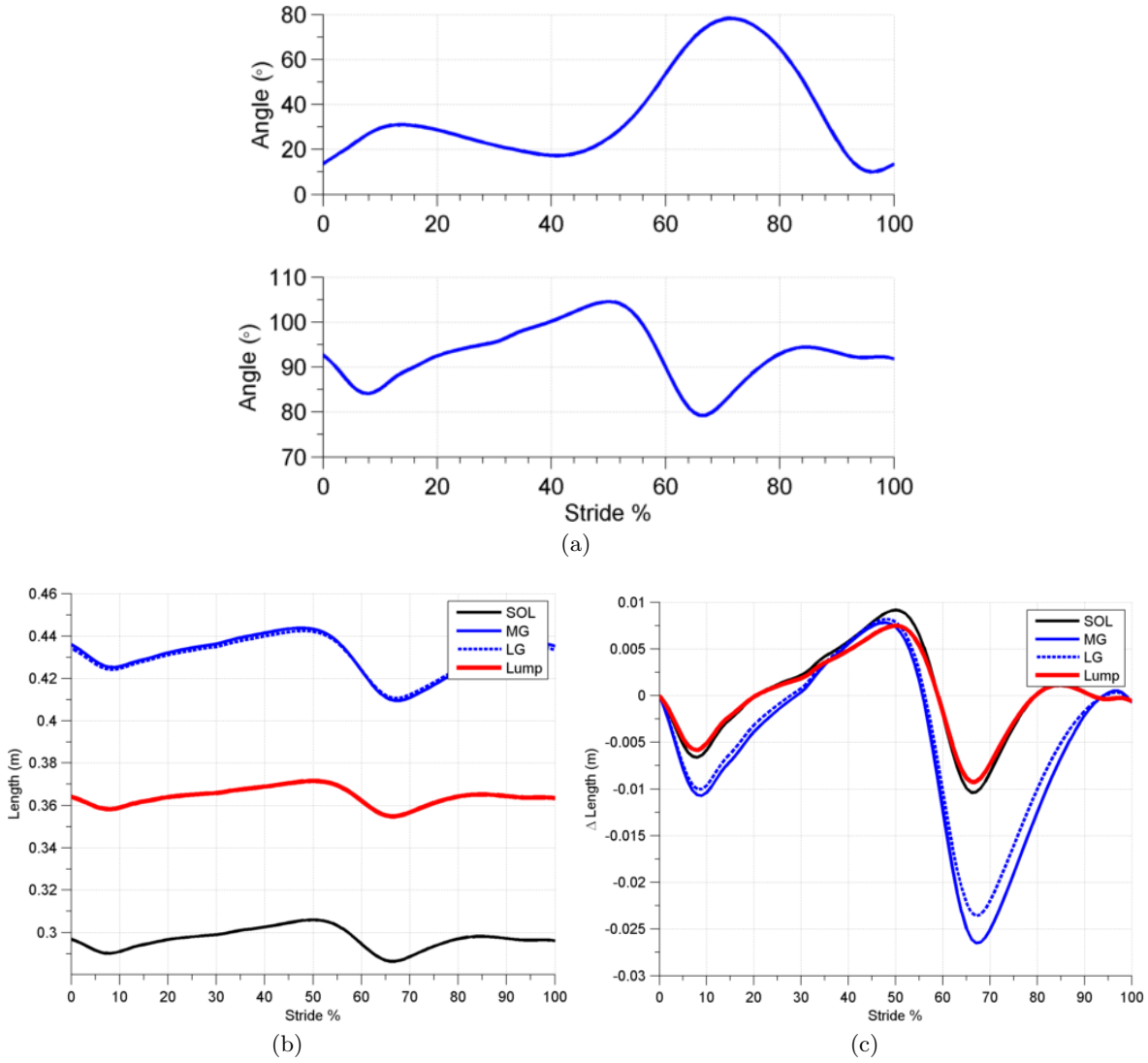

Figure A.1: **Angle profiles and length profiles for LG, MG, SOL, and lump MTUs.** a) Knee profile[top] and ankle profile[bottom] used to modulate the regression estimates. According to the Hawkins and Hull convention, 0° indicates full extension in the knee and full dorsiflexion for the ankle. b) Total lengths of each MTU for each joint angle. c) Change in lengths for each MTU for each joint angle.

length profile was assigned as the L_{CE} profile for the TA, while the EMG defined the α profile. The L_{CE_0} was set to .068 m in accordance with muscle body data from Ward et al.[64]. The $F_{CE_{MAX}}$ was set to 725 N, which was close to the Arnold and Delp model estimate of 672 N[7]. Finally, the $V_{CE_{MAX}}$ was set to be 8*L_{CE_0} [43][46][47].

Moment arm calculations were taken from Maganaris et al[49]. Maganaris demonstrated that the moment arm of the TA changed according to the force produced by the TA. The tendon of the TA does not attach directly to the ankle joint (like the triceps surae group insertion into the calcaneal tuberosity), and is instead coupled via a connective tissue feature called the extensor retinaculum that deflects according to load.

The TA L_{CE_0} was used to normalized the L_{CE} pattern taken from Cheboun et al. Then, Eq. 2.1 was used to calculate the F_{CE} for all times of the stride. The moment arm was then estimated using the moment arm for each ankle angle using the F-L coefficients. The resultant moment profile, $m_{_{DF}}$, was added to the m_{net} to predict $m_{_{PF}}$.

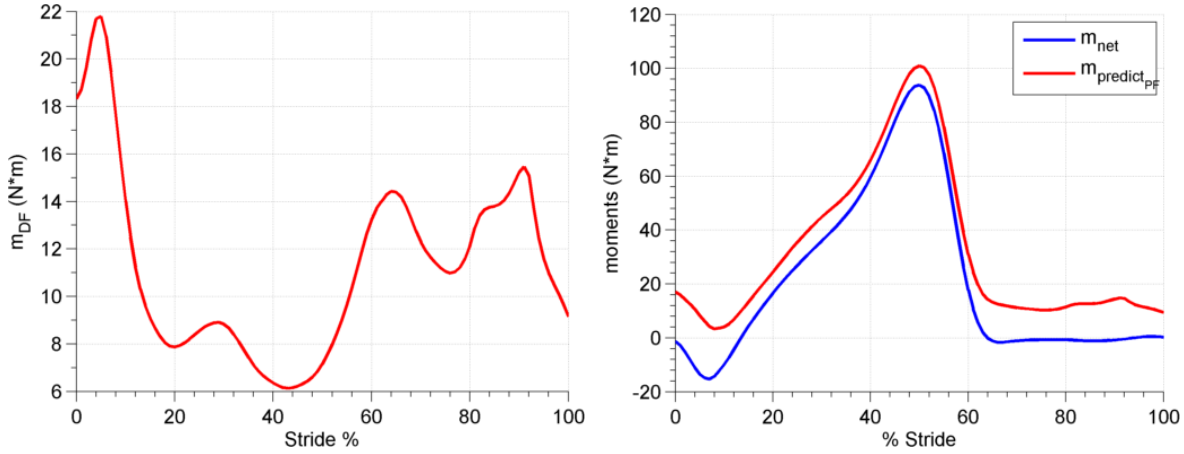

(a) (b)

Figure A.2: **TA model prediction for $m_{_{DF}}$ and $m_{_{PF}}$.** a) $m_{_{DF}}$ calculated using CE and activation profiles from Chleboun[16]. b) Prediction of $m_{_{PF}}$ created by adding $m_{_{DF}}$ to m_{net}.

Figure A.2b demonstrates that the features found in the $\vec{M}_{bio}$ and $\vec{M}_{abs}$ moment profiles(Figure 2.6a, frefts2a) are consistent with predictions from TA moment production. There is a slight toe region where PF moment declines before heel strike, minimal coactivation during the moment climax before pushoff, and significant coactivation during the swing phase.

Figure A.2a predicts that TA moment production is minimized during stance between 35 and 50% of the stride. Because m_{net} is the sum of the plantar flexor and dorsi flexor moment

profiles, it can be inferred that the plantar flexor moment profile is equal to the m_{net} profile during those portions of the stance. Ergo, any $m_{model_{PF}}(\vec{M})$ solution that did not produce an adequate moment profile between those ranges were penalized by 5 N-m for every point where the $m_{model_{PF}}(\vec{M})$ was less than m_{net} to incentivize a solution that produced as close to the m_{net} profile as possible between 35%-50% of the stride.

A.3 L_{MTU_0} vs K_t

The contour graphs in Figure 2.5 and Figure 2.7 demonstrate that the RMSE and metabolic cost are very sensitive to changes in both proportion of CE to MTU and SEE stiffness. However, these figures only indicate a sensitivity of RMSE solutions on the L_{MTU_0} plane. Because the model had 3 inputs, the volume of solution exists in 3 dimensions. Figure A.3 and Figure A.4 illustrate the RMSE and metabolic cost of $\vec{M}_{bio}$ and $\vec{M}_{abs}$ solution sets that reside orthogonally to the $\vec{M}_{bio}$ and $\vec{M}_{abs}$ solution. $^{L_{CE}}/_{L_{MTU}}$ were held constant for each case, and L_{MTU_0} and K_t were systematically varied to create the contours.

A.4 Stiffness Comparison

Table A.1: **Literature Experimental and Model Stiffness Values.**

Investigator	**Study Type**	**Tissue Type**	$\mathbf{K}_T$ (Nmm^{-1})	$\mathbf{K}_{Rot}$ $(Nm * rad^{-1})$
Hof 1998[36][37]	Experimental	Triceps Surae	351	306
Magnusson 2001[51]	Experimental	Dist. SOL APO and Tendon	469	—
		Prox. GAS APO and Tendon	486	—
de Zee 2001[18]	Experimental	Triceps Surae	—	529
Magnusson 2003[50]	Experimental	Free Tendon	759	—
Lichtwark 2005[45]	Experimental	MG/LG Common Tendon	188	—
Krishnaswamy 2011[43]	Model	GAS + SOL Connective Tissues	375.6	—
Houghton 2012[38]	Experimental	Triceps Surae	805	—
Albracht 2013[1]	Experimental	MG APO and Tendon	315	–

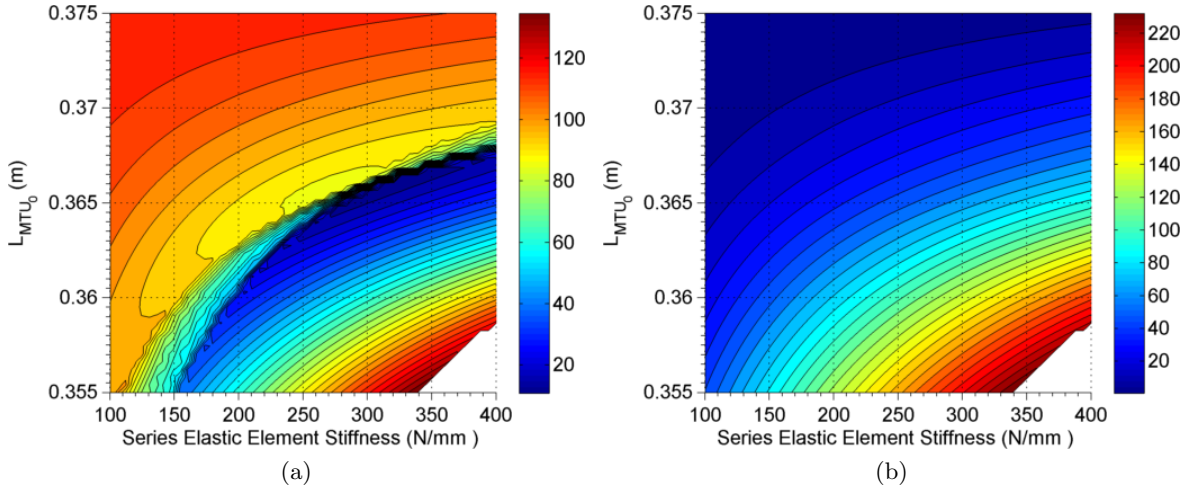

(a) (b)

Figure A.3: **Contour maps of RMSE and metabolic cost for L_{MTU_0} lengths and K_t stiffnesses surrounding $\vec{M}_{bio}$ solution.** a) RMSE contour map of solutions surrounding $\vec{M}_{bio}$ on the $^{L_{CE}}/_{L_{MTU}} = 10.8\%$ plane, and b) corresponding metabolic costs for each vector.

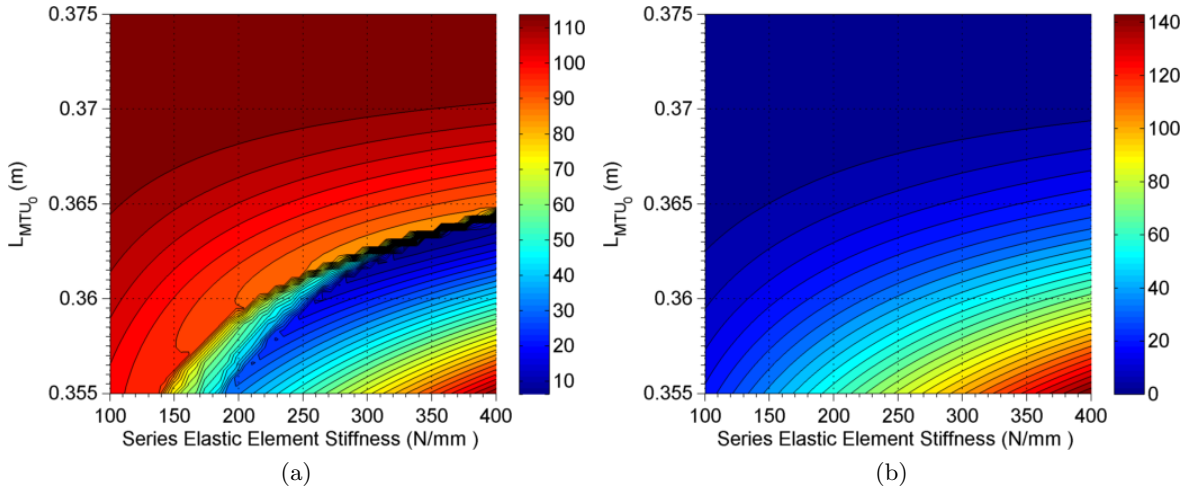

(a) (b)

Figure A.4: **Contour maps of RMSE and metabolic cost for L_{MTU_0} lengths and K_t stiffnesses surrounding $\vec{M}_{abs}$ solution.** a) RMSE contour map of solutions surrounding $\vec{M}_{abs}$ on the $^{L_{CE}}/_{L_{MTU}} = 3.67\%$ plane, and b) corresponding metabolic costs for each vector.